Master's Thesis

Ab Initio DFT Study of Catalytic and Electrochemical Nanostructures

Ji Hui Seo

Department of Energy Engineering

(Energy Engineering)

Graduate School of UNIST

2019

Ab Initio DFT Study of Catalytic and Electrochemical Nanostructures

Ji Hui Seo

Department of Energy Engineering
(Energy Engineering)

Graduate School of UNIST

Ab Initio DFT Study of Catalytic and Electrochemical Nanostructures

A thesis/dissertation
submitted to the Graduate School of UNIST
in partial fulfillment of the
requirements for the degree of
Master of Science

Ji Hui Seo

06/05/2019
Approved by

_____

Advisor
Jun Hee Lee

Ab Initio DFT Study of Catalytic and Electrochemical Nanostructures

Ji Hui Seo

This certifies that the thesis/dissertation of Ji Hui Seo is approved.

06/05/2019

signature

_____

Advisor: Jun Hee Lee

signature

_____

Kwangjin An

signature

_____

Ji Hyun Jang

Abstract

Density functional theory (DFT) is an efficient method to characterize materials because DFT calculation has a great benefit in terms of time and cost in research and can identify characteristics that cannot be observed in experiments. In this paper, I present three research results on photocatalyst, catalyst for hydrogenation and battery, which have been recently studied using DFT. In the study of photocatalyst, hematite, the host Ti doping effect observed in both experimental and theoretical studies to improve the photoelectrochemical (PEC) performance of Si doped hematite is demonstrated by coulombic attraction between Ti and polarons through electronic and structural analysis. In the research of catalyst for furfural conversion, Cu_2O has much high furfural conversion yield and selectivity due to stronger adsorption of furfural and easier hydrogen supply for furfural hydrogenation than Cu and CuO. A design of a sulfur doped silicon anode using DFT calculation suggests that chain-like poly-sulfide maintains an empty channel of low barrier for Li diffusion resulting in thousands times higher Li diffusion coefficient and that lithium sulfide also contributes to improved Li diffusivity due to an empty space formation at interface between Li_2S and amorphous Si and metallic properties by charge transfer. These studies provide insights into the analysis using DFT in various nanostructure studies.

Contents

List of Figures

Figure 1. The PEC activity in a 1 M NaOH (pH=13.6) electrolyte under simulated sunlight illumination (1 sun) of Si-doped hematite w/wo precedent Ti-doping: a) Si:Ti-Fe_2O_3 and b) Si-Fe_2O_3. c) The formation energy for Si-doping w/wo the host Ti-dopant in Fe_2O_3. A dotted vertical line represents 1 atm where the experiments were performed. d) Crystal-orbital overlap population (COOP) of Fe atoms in Si-Fe_2O_3 (d-I) and Si:Ti-Fe_2O_3 (d-II). Thicker and a greater number of yellow arrows in Si-Fe_2O_3 (vs. in Si:Ti-Fe_2O_3) represent stronger electron repulsion between Fe atoms due to the excess charges on them.

Figure 2. The co-doping configurations of (a) $\mathbf{Si_{sub}}$ and (b) $\mathbf{Si_{inter}}$ with 3d transition metal, which used to all co-doping calculations. Each is the most stable of all possible configurations in (Ti, Si) co-doping.

Figure 3. (a) The number of excess electrons which are transferred from dopants to surrounding Fe atoms in (M, Si) co-doped hematite. (b) The formation energy for guest Si doping in each host doped hematite. The upper graph is for $\mathbf{Si_{sub}}$ doping and the lower one is for $\mathbf{Si_{inter}}$ doping. Doped Si always has 4+ charge state in hematite. The number of excess electrons is changed according to the charge state of the host dopants. Each host in blue, white and yellow region have the charge state of 2+, 3+ and 4+, respectively.

Figure 4. The binding energy for (a) $\mathbf{Si_{sub}}$ and (b) $\mathbf{Si_{inter}}$ co-doping with each 3d transition metal. The binding energy of Si mono-doping is set to zero.

Figure 5. Partial charge density distributions of (a) Si mono-doping and (b-j) each (M, Si) co-doping structure for $\mathbf{Si_{sub}}$ doping. (b) M=Sc, (c) Ti, (d) V, (e) Cr, (f) Mn, (g) Co, (h) Ni, (i) Cu and (j) Zn.

Figure 6. Partial charge density distributions of (a) Si mono-doping and (b-j) each (M, Si) co-doping structure for $\mathbf{Si_{inter}}$ doping. (b) M=Sc, (c) Ti, (d) V, (e) Cr, (f) Mn, (g) Co, (h) Ni, (i) Cu and (j) Zn.

Figure 7. Partial charge density distributions of (a) (Ti, Si) co-doped and (b) $\mathbf{Si_{inter}}$ doped hematite. The distribution of polarons marked in green is different between (a) and (b). (c) Partial charge density distribution of $\mathbf{Si_{inter}}$ doped hematite with arbitrarily migrated polaron, marked in green. The polaron migration reduces a repulsion between polarons by 0.34eV.

Figure 8. Graph for binding energy versus. distances between Si and Ti for (Ti, Si) co-doped hematite. The binding energy and distance are calculated for all possible configuration of (Ti, Si) co-doping.

Figure 9. Formation energies of Si mono-doping (blue lines), (Ti, Si) co-doping (pink lines) and (V, Si) co-doping (green lines) with oxygen pressure change in 1300K. O-rich condition and Fe-rich condition are determined by restriction conditions of $\mathbf{E(Fe_2O_3)} = \mathbf{2\mu_{Fe} + 3\mu_O}$ and $\mathbf{\mu_O} = \mathbf{3E(Fe_2O_3)} - \mathbf{2E(Fe_3O_4)}$, respectively.

Figure 10. Catalytic results of FAL hydrogenation. (a) Illustration of reaction pathways and corresponding major products of FAL hydrogenation. (b) Reaction rates of FAL hydrogenation over *m*-CuO series at the reaction temperature of 180 °C. (c) FAL conversion and selectivity changes over *m*-CuO-150 as a function of reaction temperature. Reaction conditions: FAL: 1 g, isopropanol: 20 mL, catalyst: 10 mg, H_2: 20 bar, reaction temperature: 120–180 °C, reaction time: 5 h, stirring speed: 600 rpm.

Figure 11. Top (left) and side (right) views of furfural adsorbed on the (a) Cu(111), (b) CuO(100) and (c) Cu2O(100) surface structure.

Figure 12. Top view of the outmost layer of the (a) Cu(111), (b) CuO(100) and (c) Cu2O(100) surface. The minimum Cu-Cu distance of each surface is 2.568 , 2.919 and 2.429 .

Figure 13. Side (above) and top (below) view of initial configuration of (a) H2 and (b) 2H on CuO. Side view of fully-relaxed final configuration of (c) H2 and (d) 2H on Cu2O. H atoms are strongly trapped on surface oxygen atoms.

Figure 14. (a) The migration barrier of H atom on Cu2O(100) and structures along the diffusion pathway. (b) H2 TPD spectra using the heating rates of (A) 2K/min, (B) 5K/min, (C) 10K/min and (D) 15K/min. (c) $\mathbf{ln(\Phi/T_{max}^2)}$ versus $\mathbf{1/T_{max}}$ plot from H2 TPD spectra . The slope value is -6.48225.

Figure 15. (a) Scanning transmission electron microscopy (STEM) image. Corresponding energy-dispersive X-ray spectroscopy (EDS) maps for (b) Si and (c) sulfur. (d) Calculated diffusion coefficient (D_{Li}) after CV measurement that corresponds to the state after 50 cycles. (e) X-ray Photoelectron spectroscopy results of S 2*p* core-level spectra of QMS.

Figure 16. Band structure of S doped Si with different substitution doping concentrations of (a) 0.39%, S_1Si_{255}, and (b) 1.59%, S_1Si_{63}. The charge density distribution at these impurity levels (in the insets) is shown in red and blue lines to intuitively illustrate the contribution of Si to the metallic properties. The isosurface of the density is 0.0005 $\mathbf{e}/\mathbf{Å^3}$. (b) Hall effect measurement results of S doped Si.

Figure 17. (a) Initial channel structure with slab spacing of 1.18 nm (left) and its fully-relaxed channel structure without sulfur chains (right), (b) Fully-relaxed structure with the slab spacing of 0.46 nm from initial spacing range of 0.51 to 0.70 nm with sulfur chains. (c) Fully-relaxed structure with the slab spacing of 0.81 nm from initial spacing range of 0.80 to 0.99 nm.

Figure 18. (a) Sulfur chain structure under applied pressure depending on different channel sizes, as calculated by DFT. (b) Diffusion barrier of Li ion through the channel center. (c) HR-TEM image of the hollow S doped Si (inset: corresponding fast fourier transform image). (d) Enlarged TEM image showing column formation between characteristic Si (111) planes. (e) Intensity profiles of selected areas in (c).

Figure 19. (a) Schematic illustration of Li diffusion path at an interface between lithium sulfide ($\mathbf{Li_2S}$) and amorphous Si (a-Si). (b) Diffusion energy barrier for Li-ion via the interface path. (c) Band structure of the interface structure of H-passivated amorphous Si without $\mathbf{Li_2S}$ (Fermi level (E_f) set to zero) and charge density plot at CBM state (red line). White atoms on the silicon surface are hydrogen atoms. (d) Band structure of the interface structure of a-Si with $\mathbf{Li_2S}$ and charge density plot at the state across the E_f (red line). Isosurface of the density is 0.0007 $\mathbf{e}/\mathbf{Å^3}$.

1. Introduction

Density functional theory (DFT) is an efficient method to characterize materials. Because DFT deals with the materials at the atomic scale, we can predict properties that cannot be measured in experiments through the electronic, structural and optical analysis using DFT calculations. For examples, DFT can be used to compare the characteristics between an undoped system and a doped system in order to analyze in detail how a certain dopant affects the electronic properties and what structural changes caused from the doping contributes to a performance of the system. In addition, since the analysis using DFT consumes relatively short time and there is not restriction on material supply, a material proposed by DFT calculation is used for an experimental analysis. Because of these advantages, DFT has been widely used in researches of various nanostructures. In this study, I introduce the calculational methods and results of photo-catalyst, catalyst and battery design using DFT.

2. Density Functional Theory

Since an atom is composed of a large number of electrons and nuclei, the properties of materials are determined by the atomic arrangement, including the bonding of atoms mediated by the surrounding electrons. Thus, to understand the properties of a material, it is necessary to understand the behaviors of electrons and nuclei in the material. In principle, all the behaviors of electrons and nuclei are described as the Schrodinger equation, so we can get properties of the system by solving the Schrodinger equation. However, it is practically hard to solve the Schrodinger equation of a system containing many electrons and nuclei because it contains a term of the Coulombic interaction between all electrons. Thus, several approximations and theorems were suggested to solve this problem; Born-Oppenheimer approximation, Hohenberg-Kohn Theorems and Kohn-sham suggestion. The Born-Oppenheimer approximation is assumed that the nuclei move much slower than the electrons because the nucleus is much heavier than an electron, so that it is seen as fixed. Thus, we should consider a static external potential V induced by the movement of electrons in the electric field of the nucleus.

$$\boldsymbol{H = \frac{h^2}{2m}\sum_{i=1}^{N}\nabla_i^2 + \sum_{i=1}^{N}V(r_i) + \sum_{i=1}^{N}\sum_{j<i}U(r_i, r_j)}$$

The first, second and third terms describe the kinetic energy of each electron, the potential energy from the external field of charged atomic nuclei, and the interaction energy between different electrons, respectively. However, it is still difficult to solve the equation because the individual

electron wave functions associated with all the other electron are still required to determine the energy of many body system.

Hohenberg and Kohn theorems proved that

> Theorem 1. The external potential (V_{ext}) is a unique functional of the electron density (n(r)).
>
> Theorem 2. The ground state energy is the global minimum value of this functional, and the density that minimizes the total energy is the exact ground state density.

Since the wavefunction and Hamiltonian is uniquely determined by external potential, the ground state total energy and all other the ground state properties are determined by electron density. The Hohenberg-Kohn Theorems indicate that the wavefunction, Hamiltonian and electron density function are same as each other. According to the Hohenberg-Korn theorem, the total energy can be shown as follows:

$$\mathrm{E[n(r)]} = \int V_{ext}(r)n(r)dr + T[n(r)] + E_{ee}[n(r)] = \int V_{ext}(r)n(r)dr + F[n(r)]$$

F[n(r)] which consists of the terms of kinetic energy and electron-electron repulsion is a system-independent functional and exists only for the ground state electron density. Because the second theorem is the practical way to obtain the ground state density using the variational principle, the energy of system can be determined.

To obtain more exact F[n(r)] value, Kohn-Sham introduced a fictitious system with same density, that non-interacting electrons moving in effective Kohn-Sham potential. By solving Schrödinger equation using a sum of one-electron Hamiltonians, we can obtain the wavefunction of molecular orbitals and energy. Due to the invertibility between Hamiltonian and electron density, theoretically we can compute the exact density of interacting electrons. The Kohn-Sham equation is

$$\left[\frac{h^2}{2m}\nabla^2 + V(r) + V_H + V_{XC}\right]\psi_i(r) = \varepsilon_i\psi_i(r), \qquad V_{XC} = \frac{\delta E_{XC}}{\delta n(r)}$$

The equation including three different potential. $V(r)$ is external potential, V_H is coulomb potential and V_{XC} defines exchange and correlation contributions to the single-electron equation.

In Density functional theory (DFT), the total energy calculation starts with a certain electron density and is repeated until the energy becomes within the expected tolerance. Thus, the ground state total energy and any physical properties of a system with many electrons can be obtained only using ground state electron density without considering all the wave functions of each electrons.

3. Co-doping in photo-catalyst, hematite

As solar energy has attracted much attention as an alternative energy resource, research on the photoelectrochemical (PEC) water splitting reaction has recently focused on finding efficient semiconductor materials. Hematite(α-Fe_2O_3) is one of promising materials for photocatalyst with an ideal band-gap of 2.2eV[1, 2], which is appropriate for photoexcitation with visible light. It also has a lot of advantages like nontoxicity, abundance and chemical stability. However, an energy conversion efficiency of hematite cannot approach the theoretical efficiency of 12.9%[3, 4] due to the fast recombination rate[5], short hole diffusion length[1, 6] and low carrier mobility[7] by the small polaron transport.

Impurity doping is a method to improve the PEC performance of semiconductor and has been used theoretically and experimentally to compensate the disadvantages, such as adjusting the band edge or raising the carrier concentration. In previous studies, it was reported that polaron formation by doping could improve the conductivity of hematite[8, 9]. For examples, a dopant acting as an electron donor such as Ti, Si and Sn can generate small polaron by reducing Fe^{3+} to Fe^{2+} and increase the electrical conductivity via a polaron hopping mechanism[10-13]. Co-doping is an effective strategy used to increase doping solubility or carrier mobility by synergetic effects such as size balance and charge compensation between two different dopants[14, 15]. Thus, as finding an ideal co-dopants pairs that provides additional structural stability to reduce the lattice distortion, the doping concentration can further increase and improve the electrical conductivity and energy conversion efficiency. The structural stability and feasibility of any doping system can be determined by calculating doping formation energy or binding energy.

In previous experimental study, Ti-Si co-doping further enhanced the PEC performance of hematite than Si mono-doping (Fig.1a,b). In our DFT calculation, Ti-Si co-doping reduced the excess charge induced from Si doping (Fig.1d). This charge reduction decreased a repulsive force between excess charges, so that lattice distortion also decreased, resulting in decrease of Si doping formation energy (Fig.1c). The decreased formation energy means that a dopant can be distributed in hematite more uniformly. Thus, the previous study suggested that Ti-Si co-doping amplify the Si doping effect, which improves the PEC performance. To investigate the exceptional formation energy reduction in Ti-Si co-doping, we analyzed co-doping effect using Si and 3d transition metals.

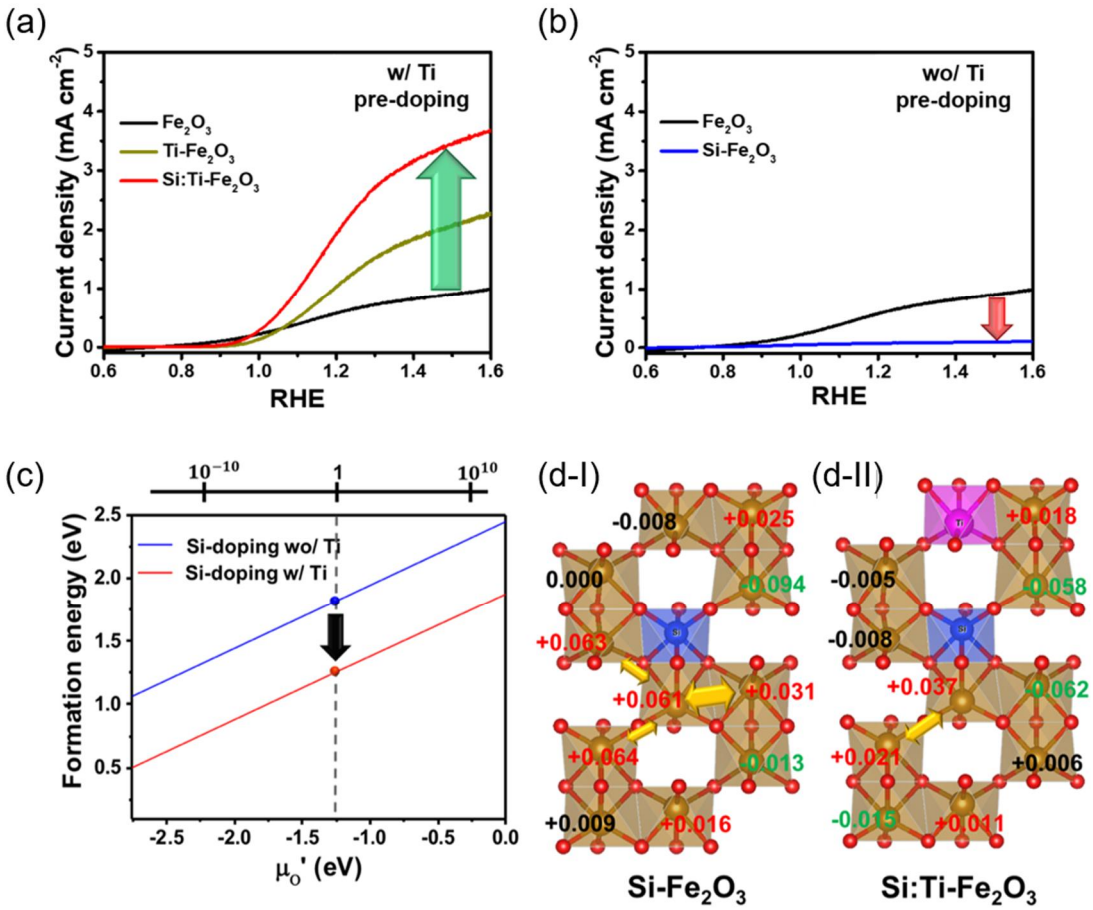

Figure 1. The PEC activity in a 1 M NaOH (pH=13.6) electrolyte under simulated sunlight illumination (1 sun) of Si-doped hematite w/wo precedent Ti-doping: a) Si:Ti-Fe_2O_3 and b) Si-Fe_2O_3. c) The formation energy for Si-doping w/wo the host Ti-dopant in Fe_2O_3. A dotted vertical line represents 1 atm where the experiments were performed. d) Crystal-orbital overlap population (COOP) of Fe atoms in Si-Fe_2O_3 (d-I) and Si:Ti-Fe_2O_3 (d-II). Thicker and a greater number of yellow arrows in Si-Fe_2O_3 (vs. in Si:Ti-Fe_2O_3) represent stronger electron repulsion between Fe atoms due to the excess charges on them.

3.1 Calculational methods

Si and each 3d transition metal (noted as M) were used as a guest dopant and a host dopant, respectively, to identify the synergetic effect of Si and 3d transition metal pairs in terms of structural stability in hematite. The host doping effect was confirmed by comparing formation energy of each (M, Si) co-doping based on formation energy of Si mono-doping. When the host M is substitutionally doped in the Fe2O3 unit cell containing 12 Fe atoms and 18 O atoms, there are symmetrically distinct 11 substitutional doping sites and 6 interstitial doping sites for the guest Si doping. There are various factors can contribute to structural stability. For examples, as will be discussed below, a different polaron distribution can bring some stabilization by changing an electrostatic repulsion between polarons. Therefore, we considered only one co-doping configuration to minimize the factors. The most stable configurations in the (Ti, Si) co-doping system were used for the calculations and each co-doping configuration for guest Si substitutional (Si_{sub}) and interstitial doping (Si_{inter}) is shown in Fig.2.

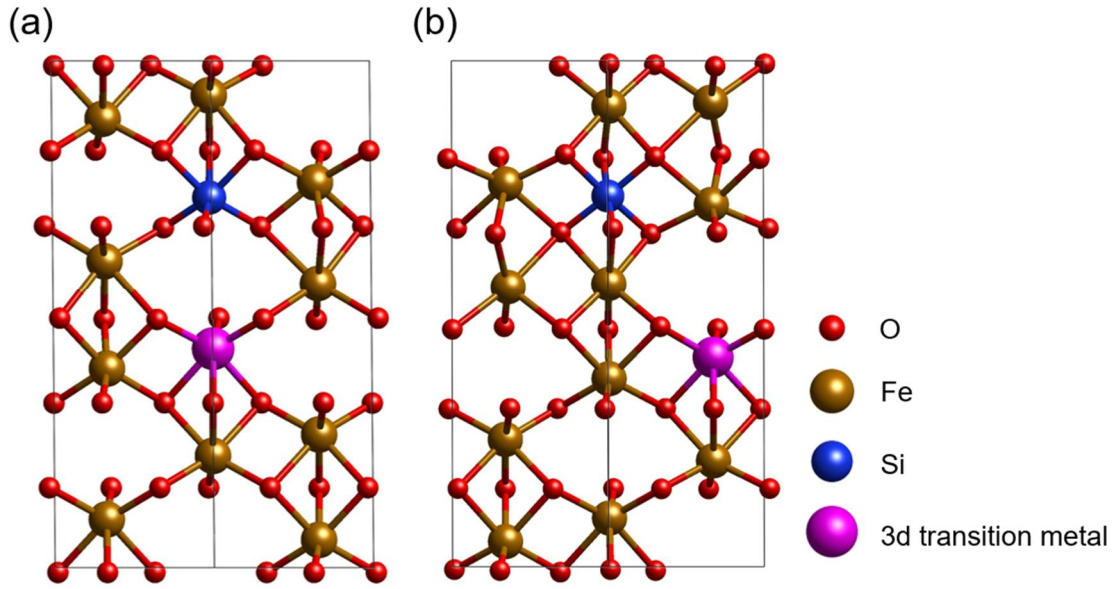

Figure 2. The co-doping configurations of (a) $\mathbf{Si_{sub}}$ and (b) $\mathbf{Si_{inter}}$ with 3d transition metal, which used to all co-doping calculations. Each is the most stable of all possible configurations in (Ti, Si) co-doping.

The formation energy (ΔE_f) was calculated to identify the structural synergetic effects. The formation energies for Si_{sub} and Si_{inter} mono-doping are expressed as follows[12]:

$$\Delta E_f(Si_{sub}\ \text{doped}) = E(Si_{sub}:Fe_2O_3) - E(Fe_2O_3) - \mu_{Si} + \mu_{Fe},\ y=0.083$$

$$\Delta E_f(Si_{inter}\ \text{doped}) = E(Si_{inter}:Fe_2O_3) - E(Fe_2O_3) + \mu_{Fe},\ y=0.083$$

$E(Si_{sub}:Fe_2O_3)$, $E(Si_{inter}:Fe_2O_3)$ and $E(Fe_2O_3)$ are the total energies of the fully-relaxed Si_{sub}, Si_{inter} doped and pristine Fe_2O_3, respectively. μ_{Si} and μ_{Fe} are the chemical potentials of Si and Fe atoms, respectively. According to the definition of the formation energy, the formulas include a term related to the charge state, but this term was ignored because there is no change in the number of electrons in the calculating systems.

In cases of Si_{sub} and Si_{inter} co-doping with 3d transition metal M, the formation energies are shown as below:

$$\Delta E_f(Si_{sub}\ \text{doped w/ M}) = E(M, Si_{sub}:Fe_2O_3) - E(M:Fe_2O_3) - \mu_{Si} + \mu_{Fe}$$

$$\Delta E_f(Si_{inter}\ \text{doped w/ M}) = E(M, Si_{inter}:Fe_2O_3) - E(M:Fe_2O_3) + \mu_{Fe}$$

$E(M, Si_{sub}:Fe_2O_3)$ and $E(M, Si_{inter}:Fe_2O_3)$ are the total energies of the fully-relaxed Si_{sub}, Si_{inter} co-doped Fe_2O_3 with M respectively and $E(M:Fe_2O_3)$ is the total energy of the fully-relaxed M mono-doped Fe_2O_3. We focused on the effect of the precedent host M doping on the guest Si doping, so the M doped system was used as a reference system to calculate the formation energies of the co-doping systems. Thus, in (M, Si) co-doping, the lower formation energy means that how much the host stabilize the guest Si doping.

The binding energy usually represents an interaction between co-dopant pairs and is defined as[16]

$$E_B = \Delta E_f(Si\ \text{doped}) + \Delta E_f(M\ \text{doped}) - \Delta E_f(M, Si\ \text{codoped})$$

Since the co-dopants do not bond directly to each other in our calculations, the binding energy implies a degree of structural stabilization by co-doping with various factors. When the above formula is combined with the formation energy equations, it is rearranged as below:

$$E_B = E(Si:Fe_2O_3) + E(M:Fe_2O_3) - E(M, Si:Fe_2O_3) - E(Fe_2O_3)$$

This equation is equal to an equation for the difference between the formation energies of (M, Si) co-doping and that of Si mono-doping. Thus, the binding energy represents the strength of additional structural effects such as attraction (positive value) or repulsion (negative value) in the co-doping system as compared to the Si mono-doping system.

In this study, we only focused on O-rich growth condition because the formation energy difference between the co-doping systems is consistent in both O-rich and Fe-rich conditions. Under O-rich condition, the chemical potential of oxygen (μ_O) is half of the total energy of O_2 molecule. However, due to the O_2 overbinding error in the GGA function[17], we used the total energy of O_2 corrected by the experimental O_2 binding energy of -5.23 eV[18] and the μ_O was determined to be -4.16eV. Under O-rich condition, the chemical potentials of Fe (μ_{Fe}) and Si (μ_{Si}) should satisfy the following restriction conditions.

$$E(Fe_2O_3) = 2\mu_{Fe} + 3\mu_O$$

$$E(SiO_2) = \mu_{Si} + 2\mu_O$$

where $E(SiO_2)$ are the total energy of SiO_2 bulk structure.

All calculational results are performed at 0K and 1bar, but other conditions can be considered using some equations related to μ_O[18, 19]. Since the μ_{Fe} and μ_{Si} are determined by the μ_O from the restriction conditions, the change of the μ_O with temperature T and oxygen partial pressure p results in the change of formation energy. The final equation of μ_O at certain T and p is summarized as follows:

$$\mu_O = \frac{1}{2}[\mu_{O_2} + \Delta H - T\Delta S + k_B T \ln\frac{p}{p^\circ}]$$

where μ_{O_2} is the total energy of O_2 molecule. ΔH and ΔS are the enthalpy and entropy changes per molecule between T and K at the standard pressure 1bar, respectively, and are taken from the thermochemical tables[20]. We define the additional terms with the enthalpy, entropy and pressure as μ'_O.

All calculations were performed in the framework of the spin-polarized density functional theory using the Vienna ab-initio simulation package (VASP) code[21]. The projector augmented wave (PAW) method was employed to describe the ion-electron interactions[22]. The exchange-correlation was considered using the generalized gradient approximation of Perdew, Burke and Ernzerhof (PBE)[23]. The cut-off energy for the plane wave basis set was 500eV to expand the electronic wave function, and Monkhorst-Pack k-point mesh[24] of 4x4x1 was used for all (1x1x1) doping structures. The ionic positions were relaxed until the Hellmann-Feynman forces reach 0.01eV/ . Because of the strongly correlated 3d states in transition metal oxide systems, we used the GGA+U framework to correct the electron self-interaction[17]. The values of U-J of all the 3d metals were set to 4.2 eV for good agreement with the experimental band-gap of α-Fe2O (2.2eV)[1, 2]. The hexagonal unit cell of α-Fe_2O_3 was fully-relaxed with a layered anti-ferromagnetic (AFM) ordering[25] and the calculated lattice

parameters of pristine hematite were of a=b=5.07□ and c=13.88□, consistent with the experimental values of a=5.04□ and c=13.75□[26].

The number of excess electrons that transfers from dopants to surrounding Fe atoms was figured out from change in calculated magnetic moments of Fe atoms. The transfer decreases the magnetic moment of Fe by reducing Fe^{3+} with five d electrons to Fe^{2+} with six d electrons. Therefore, we can take the number and positions of the excess electrons by checking the reduced Fe atoms with smaller magnetic moment than that of Fe^{3+}.

3.2 Results and Discussion

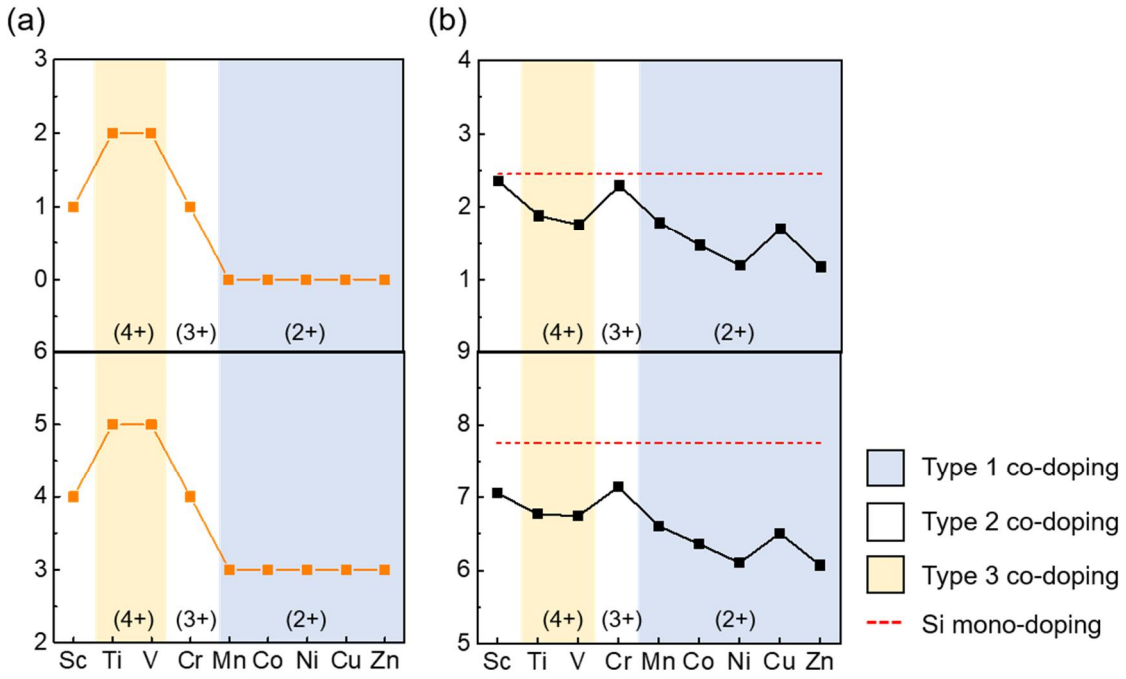

Figure 3. (a) The number of excess electrons which are transferred from dopants to surrounding Fe atoms in (M, Si) co-doped hematite. (b) The formation energy for guest Si doping in each host doped hematite. The upper graph is for $\mathbf{Si_{sub}}$ doping and the lower one is for $\mathbf{Si_{inter}}$ doping. Doped Si always has 4+ charge state in hematite. The number of excess electrons is changed according to the charge state of the host dopants. Each host in blue, white and yellow region have the charge state of 2+, 3+ and 4+, respectively.

The co-doping systems were divided into three types depending on oxidation state for each host. The number of excess electrons and the formation energy of each (M, Si) co-doped hematite are shown in Fig.3a. Because guest Si is an electron donor to prefer a 4+ charge state, Si releases one excess electron for Si_{sub} doping and four excess electrons for Si_{inter} doping to surrounding Fe atoms.

Nevertheless, in case of co-doping with host Mn, Co, Ni, Cu, and Zn, only 0 electron for Si_{sub} doping and 3 electrons for Si_{inter} doping are observed (Fig.3a). This means that one electron released by the Si flows to the host metal, not Fe atom. Thus, the corresponding 3d transition metals act as electron acceptors and exist in 2+ state (Fig.3, blue region). For the same reason, in case of co-doping with the same number of excess electrons as in Si mono-doping, the host metals have 3+ states (Fig.3, white region, M=Sc, Cr), and in case of co-doping with one more electron than Si mono-doping, the hosts are electron donors and have 4+ states in hematite (Fig.3, yellow region, M=Ti, V). We defined the co-doping with the hosts of 2+, 3+ and 4+ state as A-D (Acceptor-Donor), N-D (None-Donor) and D-D (Donor-Donor), respectively.

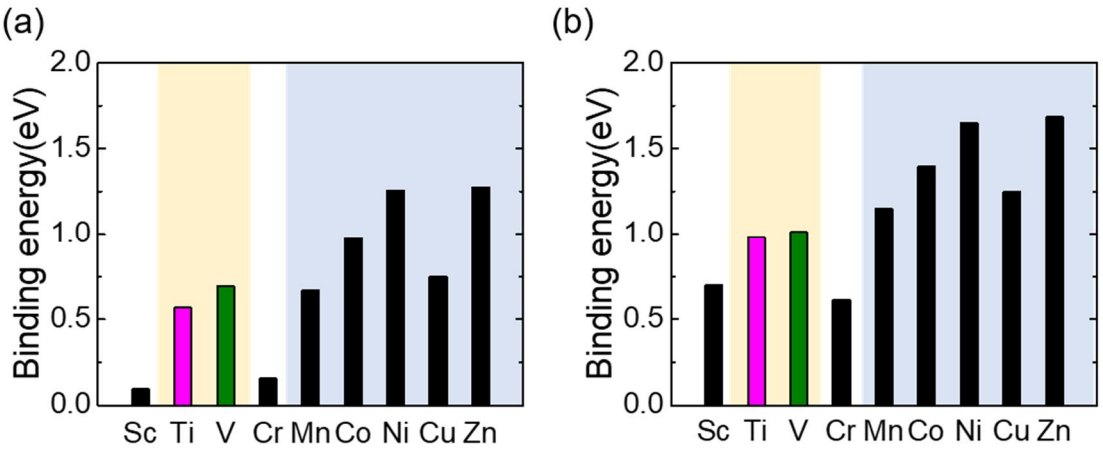

Figure 4. The binding energy for (a) $\mathbf{Si_{sub}}$ and (b) $\mathbf{Si_{inter}}$ co-doping with each 3d transition metal. The binding energy of Si mono-doping is set to zero.

Counterintuitively, we found the largest excess electron doping group of D-D can be stabilized. Obviously, increasing excess electrons makes the structure unstable due to repulsive forces. Thus, it was expected that the formation energies are higher in order of D-D, N-D and A-D in which the excess electrons increase. However, D-D has unexpectedly low formation energy and the formation energies are higher in order of N-D > D-D > A-D (Fig.3b). The binding energies also represent that the D-D co-doping causes a high structural stability as much as charge compensation effect of A-D (Fig.4). Thus, host Ti and V in D-D co-doping have some structure stabilization effect.

To investigate the stabilization effect induced in host Ti/V and guest Si co-doping, polaron distribution of each type of co-doping system was analyzed with its binding energy using partial charge density. Since all systems use the same co-doping configuration, each type of co-doping structures has the same polaron distribution (Fig.5 for Si_{sub} and Fig.6 for Si_{inter}). Interestingly, for Si_{inter} doping, co-doping structures have different polaron distributions with Si mono-doping structure. To emphasize the different position of a polaron between Si_{inter} doping and (Ti/V,Si_{inter}) co-doping, the

corresponding polarons are shown with green color in Fig.25. The polaron located directly above Si dopant in Si mono-doping (Fig.7b, green) moves to an adjacent Fe site in the same layer in D-D (Fig.7a, green). We consider the origin of stabilization from D-D co-doping with three candidates of polaron dispersion, interaction between the guest and the host, interaction between the polarons and the host. Among the candidates, the last one is the origin of stabilization from D-D co-doping and the reason will be described below.

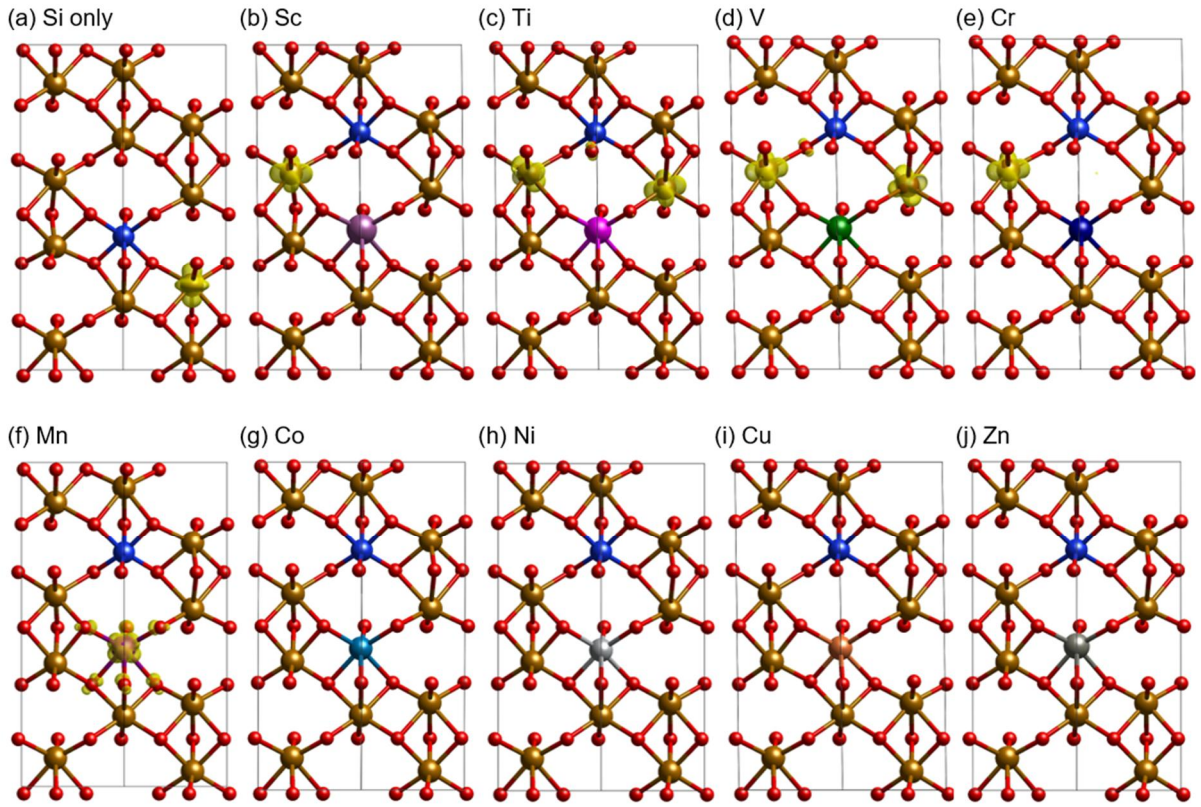

Figure 5. Partial charge density distributions of (a) Si mono-doping and (b-j) each (M, Si) co-doping structure for $\mathbf{Si_{sub}}$ doping. (b) M=Sc, (c) Ti, (d) V, (e) Cr, (f) Mn, (g) Co, (h) Ni, (i) Cu and (j) Zn.

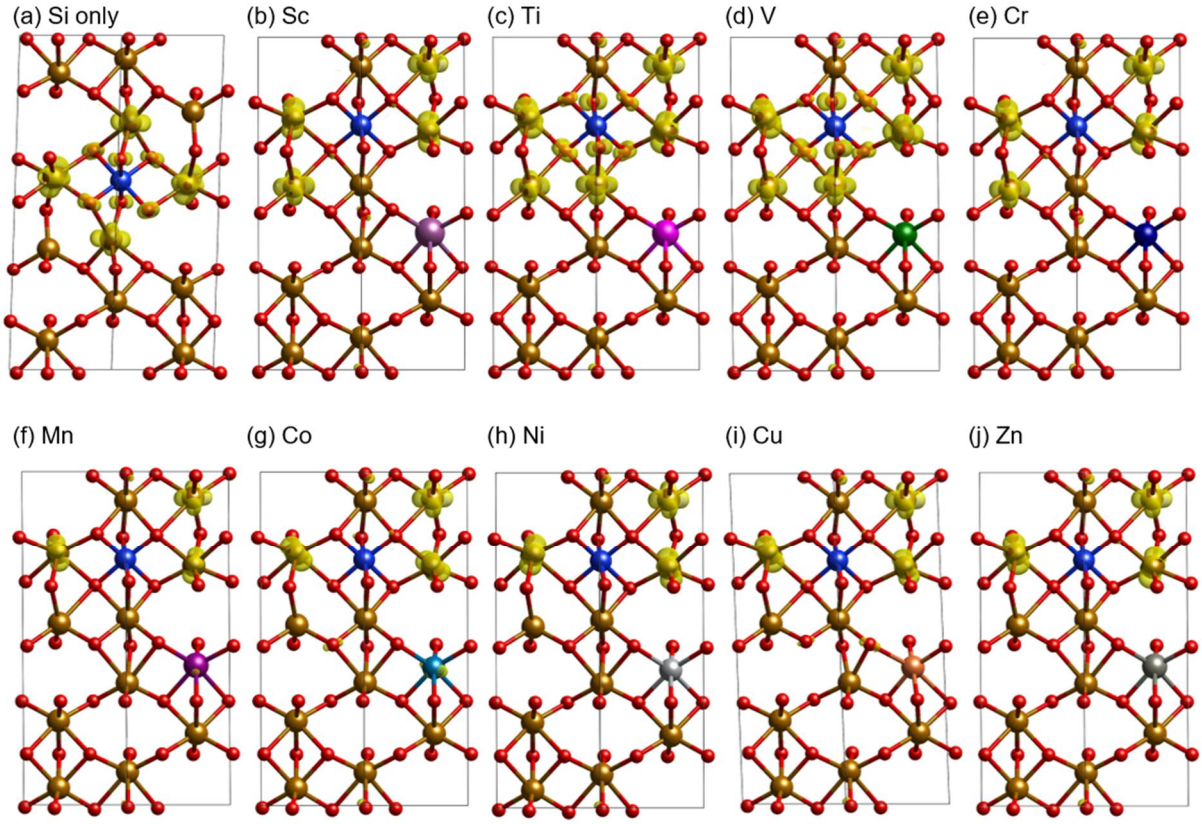

Figure 6. Partial charge density distributions of (a) Si mono-doping and (b-j) each (M, Si) co-doping structure for $\mathbf{Si_{inter}}$ doping. (b) M=Sc, (c) Ti, (d) V, (e) Cr, (f) Mn, (g) Co, (h) Ni, (i) Cu and (j) Zn.

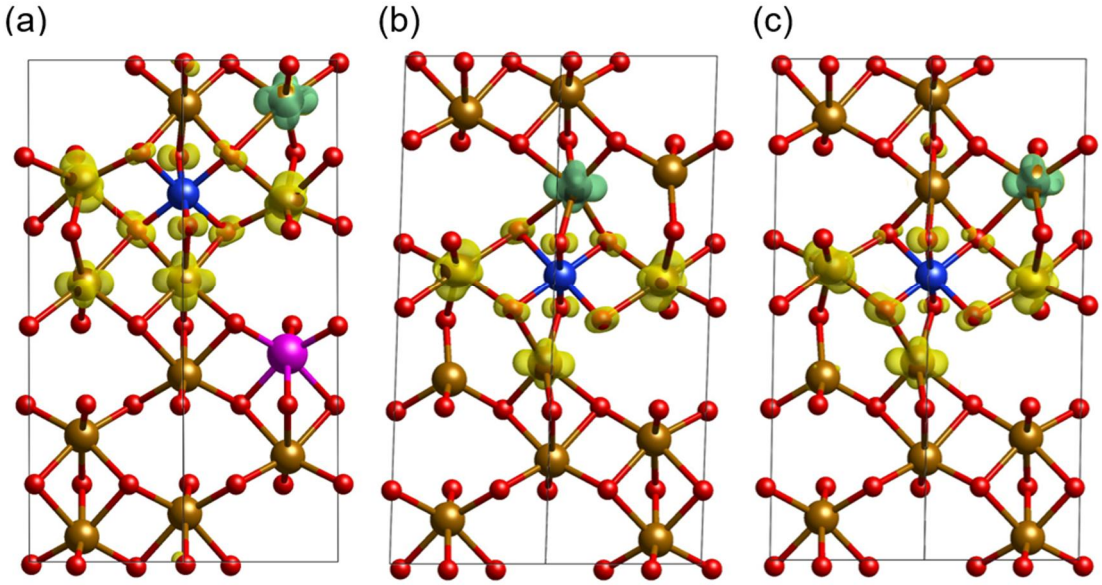

Figure 7. Partial charge density distributions of (a) (Ti, Si) co-doped and (b) $\mathbf{Si_{inter}}$ doped hematite. The distribution of polarons marked in green is different between (a) and (b). (c) Partial charge density distribution of $\mathbf{Si_{inter}}$ doped hematite with arbitrarily migrated polaron, marked in green. The polaron migration reduces a repulsion between polarons by 0.34eV.

The first candidate, polaron dispersion, decreases the repulsion between polarons, but the effect is not enough to explain binding energy. When D-D polaron distribution is applied to Si_{inter} mono-doping by moving the green colored polaron (Fig.7c), the change stabilizes the system by 0.34eV due to the reduced repulsion. In Fig.5, for Si_{inter} doping, the polaron generated by Ti and V doping is placed under Si where other polarons were gathered. Due to this additional polaron, a strong repulsion is exhibited in D-D. Thus, the stabilization induced by host doping must be larger than the repulsive force because of the positive biding energy of D-D. However, the polaron dispersion effect of 0.34 eV is not large enough to have the binding energy (1.0eV for Si_{inter}) and was not seen in Si_{sub} doping. Therefore, the polaron distribution change is not main effect for the exceptional stabilization in D-D.

There is no additional evidence of interaction between guest and host except for the fact that the host doping effect is observed only in D-D. If the interaction has main contribution to the stabilization, the binding energy should be related to distance between the co-dopants. We calculated the binding energies of all possible (Ti, Si) co-doping configurations with various distances between co-dopants, in hematite unit cell, but there was no relationship between the binding energy and the distance (Fig.8). Thus, we can conclude that the exceptional structural stability results from the interaction between the polarons and the host.

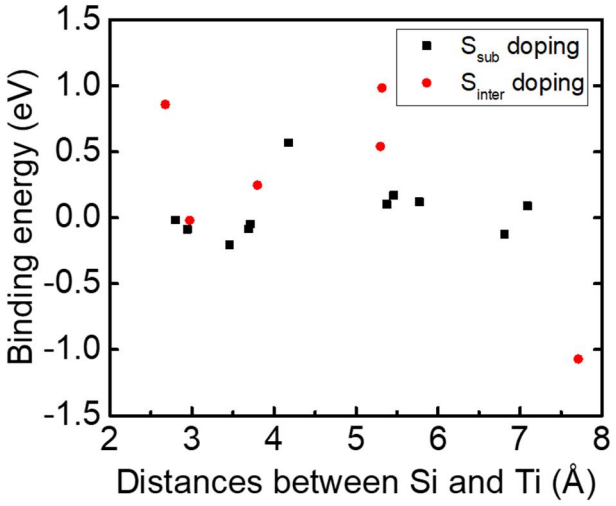

Figure 8. Graph for binding energy versus. distances between Si and Ti for (Ti, Si) co-doped hematite. The binding energy and distance are calculated for all possible configuration of (Ti, Si) co-doping.

The interaction is associated with a charge density of each polaron and host in hematite. Ti^{4+} and V^{4+} formed by giving electrons to Fe atoms are relatively positively charged as compared with surrounding Fe^{3+}. On the other hand, the small polarons localized to Fe atoms receiving electrons from the dopants are relatively negatively charged with high charge densities. There is an electrostatic attraction between the hosts and the polarons with opposite charge, and this attraction reduce the repulsion between polarons. The highly positive binding energy of the D-D co-doping system indicates that the attraction is much larger than the additional repulsion caused by the electron transfer of the hosts. Thus, the electrostatic attraction between the negatively charged polarons and positively charged hosts contributes significantly to the stabilization of Si doping in the co-doping. As a result, the preference of Ti and V for the 4+ charge state in hematite makes both additional polaron formation and increased Si doping concentration. Therefore, the different charge state of host is key factor for the strong electrostatic attraction, so that carrier concentration and guest Si doping concentration can be further improved in hematite.

The host Ti and V provide a stable environment for polaron formation. In particular, the additional formation of two and five polarons for Si_{sub} and Si_{inter} co-doping wil result in a great increase in carrier concentration. Previous experimental study has reported the increase in carrier concentration in (Ti, Si) co-doping[27]. Zhang et al. suggested that Si and Ti co-doping further enhance the donor concentration than Si and Ti mono-doping due to balancing the ion radius difference. However, they did not provide evidence for the size effect and just focused on improving PEC performance by co-doping. Based on the analysis of synergetic effect for various co-doping systems using DFT calculations, we suggest

that the carrier concentration enhancement in (Ti, Si) co-doping is caused by the interaction between polarons and Ti^{4+}.

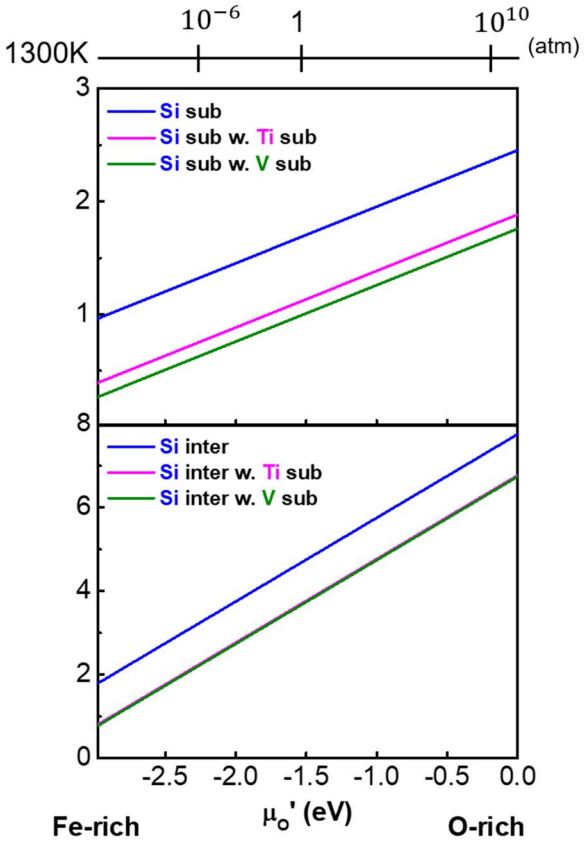

Figure 9. Formation energies of Si mono-doping (blue lines), (Ti, Si) co-doping (pink lines) and (V, Si) co-doping (green lines) with oxygen pressure change in 1300K. O-rich condition and Fe-rich condition are determined by restriction conditions of $\mathbf{E(Fe_2O_3)= 2\mu_{Fe} + 3\mu_O}$ and $\mathbf{\mu_O= 3E(Fe_2O_3) - 2E(Fe_3O_4)}$, respectively.

Even though the hosts Ti and V stabilize Si_{inter} doping as much as 1.0eV, the formation energy of Si_{inter} doping is still high. However, since the formation energy was calculated at 0K and 1bar, it can be much lower under actual experimental conditions. Fig.9 shows the formation energies for Si mono-doping and (Ti/V, Si) co-doping at 1300K with varying oxygen pressure. High temperature and low oxygen pressure experimental conditions with the hosts Ti and V make the formation energy of Si_{inter} doping as low as possible in experiments. The formation energy of Si_{sub} doping is still lower than that of Si_{inter} doping. However, because the formation energy for Si_{inter} doping decreases faster than that for Si_{sub} doping as the pressure is lowered, a difference between the formation energies for Si_{sub} and Si_{inter} doping is reduced. Thus, Si_{inter} doping ratio can be higher in proportion to the reduced difference. Therefore, using high temperature and low oxygen pressure, we can maximize the Si_{inter} doping effect to increase the carrier concentration.

4. Copper Oxide Catalyst for Furfural Conversion

Furan compounds, one of unsaturated oxygenate, has been attracting much attention due to the increased interest in the unsaturated oxygenate because of the prevalence of these compounds as intermediates in the conversion of biomass to fine chemicals and fuels (ref). Furfural is one of the abundant oxygenated compounds because it can be driven from various agricultural by-products and has a potential as a biofuel because its hydrogenation products such as 2-methyfuran and furfuryl alcohol are potential fuel. Therefore, recently, a catalyst having a high furfural conversion yield and selectivity has been studied. In our experiments, we found that cooper oxide catalyst which is reduced in hydrogen at 150°C (m-CuO-150) has a much higher furfural conversion yield and selectivity to furfuryl alcohol than the un-reduced CuO (Fig.10). To investigate the change in catalytic activity, I assumed that the reduced cooper oxide material is Cu_2O and compared furfural adsorption and hydrogen adsorption characteristics on Cu, CuO and Cu_2O surface using DFT.

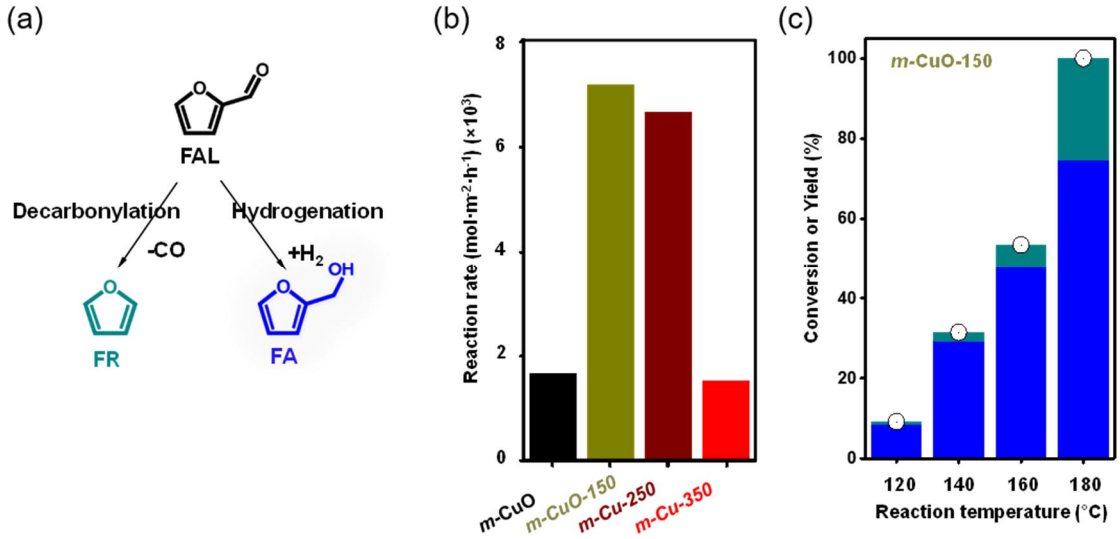

Figure 10. Catalytic results of FAL hydrogenation. (a) Illustration of reaction pathways and corresponding major products of FAL hydrogenation. (b) Reaction rates of FAL hydrogenation over *m*-CuO series at the reaction temperature of 180 °C. (c) FAL conversion and selectivity changes over *m*-CuO-150 as a function of reaction temperature. Reaction conditions: FAL: 1 g, isopropanol: 20 mL, catalyst: 10 mg, H_2: 20 bar, reaction temperature: 120–180 °C, reaction time: 5 h, stirring speed: 600 rpm.

4.1 Calculational methods

All calculations were carried out in the framework of the spin-polarized DFT using the Vienna ab

initio simulation package (VASP) with the projector-augmented wave (PAW) method[21, 22]. The generalized gradient approximation of Perdew–Burke–Ernzerhof (PBE) was used to consider exchange-correlation[23]. The cut-off energy for plane wave basis set was 500 eV and the ionic positions of all structures were relaxed until the force converges to below 0.01 eV $^{-1}$. In order to study the adsorption properties of furfural and hydrogen, the (4×4), (2×2) and (3×2) super-cells were used for Cu(111), CuO(100) and Cu_2O(100) surfaces with four Cu layers. The vacuum between slabs along the *z*-direction was set at a minimum of 12 to minimize interactions between the slabs and reduce the amount of calculation. The bottom two Cu layers of all slab system were fixed to the corresponding bulk-optimized positions. Since Cu metal system with U lose its metallic property significantly, all systems did not have U value to compare their properties. All calculations considered spin polarization to set Cu and Cu_2O to ferromagnetic and CoO to type antiferromagnetic[28]. The climbing image nudged elastic (cNEB) method was used to calculate the migration barriers of H+ on expected diffusion pathways[29]. The adsorption energy (E_{ads}) of furfural on a certain surface was calculated as $E_{ads}(FAL) = E(slab + FAL) - E(slab) - E(FAL)$, where $E(slab + FAL)$, $E(slab)$ and $E(FAL)$ are the total energies of FAL adsorbed surface structure, a clean surface and FAL, respectively.

4.2 Results and Discussion

To investigate the active phase of copper oxide, which has a crucial effect on FAL hydrogenation in the experiment, the adsorption of FAL and migration behavior of hydrogen on the Cu, CuO and Cu_2O crystal surfaces were calculated using DFT. CuO(111) and Cu_2O(111) are the most stable surfaces[30, 31], but highly reactive polar CuO(100) and Cu_2O(100) surfaces are used in our calculations. Tasker reported that unstable surface with dipole moments can only be stabilized by substantial reconstruction[32]. Thus, surface oxygen vacancies are formed by surface reconstruction of the polar CuO(100) and Cu_2O(100), and act as active sites for surface reaction due to the vacant bonding of the surround metals. Therefore, we focused on the adsorption of FAL and hydrogen on the active oxygen vacancy sites on CuO(100) and Cu_2O(100).

The furfural adsorption on Cu_2O(100) is stronger than that on Cu(111) and CuO(100). Since Cu metal has a filled *d*-orbital, a repulsive force develops between *d*-orbital of Cu and *p*-orbital of the furan ring of FAL and FAL adsorption on the Cu metal prefers an "upright" configuration perpendicular to the Cu surface without adsorption of the furan ring[33]. Thus, we considered FAL adsorption only through the terminal oxygen atom on all Cu, CuO and Cu_2O. Depending on the regularity of each surface structure, we placed the terminal oxygen of FAL at an position that connects three triangular Cu atoms on CuO(100) and diagonally connects Cu atoms on Cu_2O(100). The

adsorption energy on Cu(111) is -0.168 eV with one Cu–O bond consistent with previous DFT studies[34] (Fig.11a). On CuO(100) and Cu_2O(100), FAL has the adsorption energy of -0.719 eV and -1.630 eV, respectively (Fig.11b,c). Although FAL is adsorbed through two Cu–O bonds on both CuO(100) and Cu_2O(100) surfaces, the top Cu^+ atoms of Cu_2O(100) result in stronger FAL adsorption to Cu_2O(100) than CuO(100). Thus, the reaction probability of FAL on Cu_2O(100) increases with strong FAL adsorption, which is consistent with the experimental results of conversion higher over *m*-CuO-150 with abundant Cu_2O(100) surfaces than *m*-CuO.

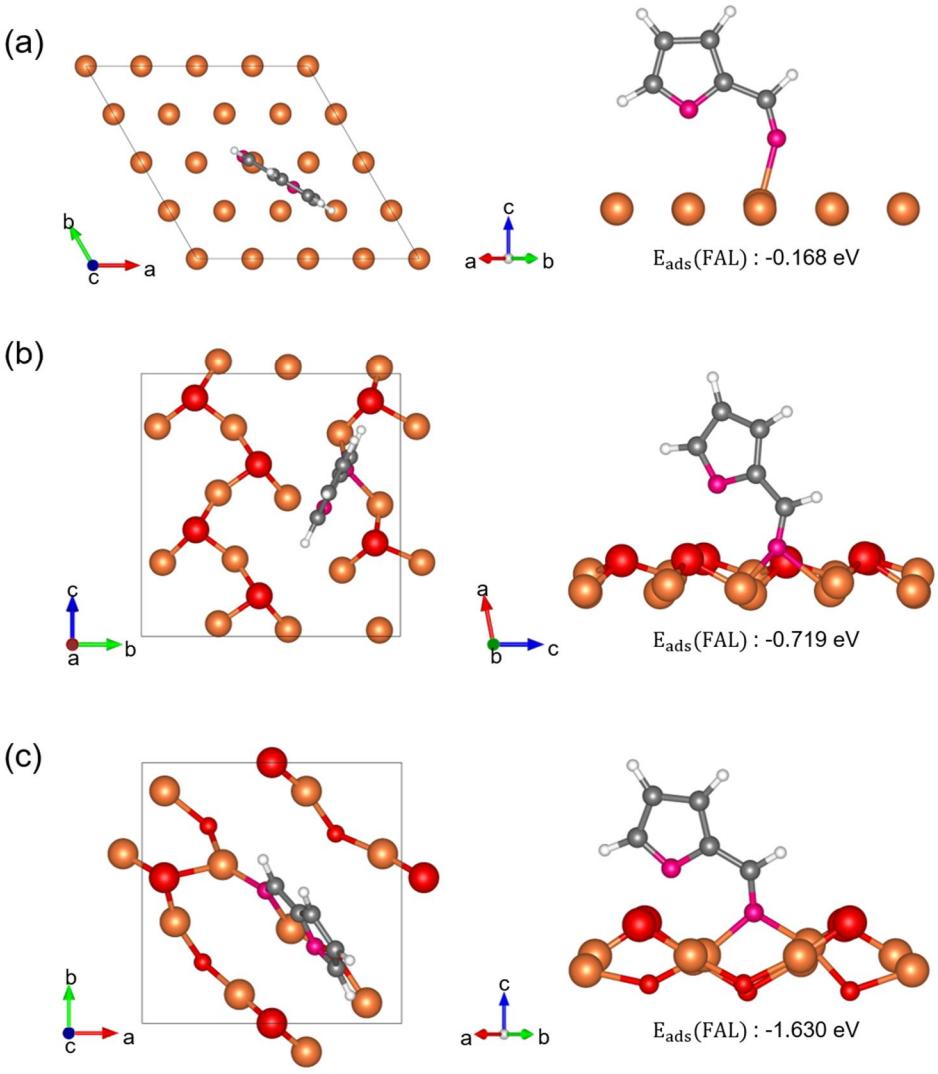

Figure 11. Top (left) and side (right) views of furfural adsorbed on the (a) Cu(111), (b) CuO(100) and (c) Cu2O(100) surface structure. (Colors : Cu/orange, C/gray, H/white, O/red, O in the outmost layer/red with large radius, O in furfural/pink)

To intuitively understand the surface structure, we represent the outermost layers of Cu(111) and CuO(100), and Cu_2O(100) consisting of the outermost Cu layer and two outer O layers in Figure 30. The oxygen atoms in the outermost layer are distinguished by having a larger radius than the other oxygen atoms. The Cu(111) surface has a constant distance between Cu atoms (Cu–Cu distance) of 2.568 Å. The CuO(100) surface with oxygen vacancies has a reconstruction structure with a surface oxygen at the center between triangular Cu atoms making three Cu–O bonds. The shortest Cu–Cu distance among oxygen-deficient Cu triangles is 2.919 □. In the Cu_2O(100) surface structure, the oxygen atoms of the two-outer layers connect the outermost Cu atoms obliquely and the structure is most stable with two oxygen vacancies at the same diagonal. The shortest Cu–Cu distance with oxygen vacancy is 2.429 □. In previous studies, H_2 could be almost spontaneously adsorbed on the surface of metallic Cu with a low dissociation energy barrier[35]. Because moderately small distance between surface Cu atoms makes hydrogen easily attach to both Cu atoms, we expected that Cu_2O(100) with oxygen vacancies can induce dissociative adsorption of H_2 more easily than Cu(111) due to shorter Cu–Cu distance of Cu_2O(100) than that of Cu(111) and CuO(100) having a Cu–Cu distance of 0.351 □ is longer than Cu(111) has the low adsorption capacity of H_2.

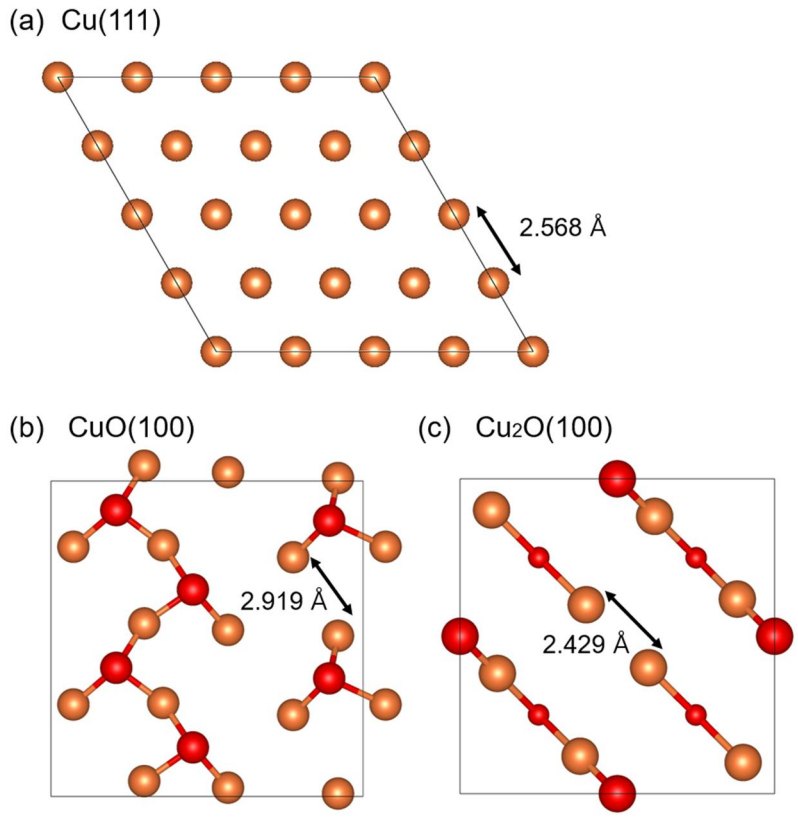

Figure 12. Top view of the outmost layer of the (a) Cu(111), (b) CuO(100) and (c) Cu2O(100) surface. The minimum Cu-Cu distance of each surface is 2.568 □, 2.919 □ and 2.429 □.

As we expected, H_2 easily attaches to Cu_2O surface in DFT calculation. To compare the adsorption properties of H_2 on CuO(100) and Cu_2O(100) surfaces, H_2 and $2H^+$ are arranged between Cu metals with the shortest Cu–Cu distance on CuO(100) (Fig.13b) and Cu_2O(100) (Fig. 13a). In a fully-relaxed structure, on CuO(100), H_2 cannot be adsorbed on the surface and $2H^+$ are strongly trapped on the surface oxygen atoms with high H adsorption energy of -1.615 eV. However, on Cu_2O(100), H_2 and $2H^+$ are adsorbed in the same configuration with a low H adsorption energy of -0.180 eV between the Cu atoms, and the bond length between two H atoms increases from 0.750 □ to 0.942 □, which is long enough to dissociate H_2 (Fig.14a, F structure). Therefore, unlike CuO surface on which hydrogen cannot migrate due to its strong bonding on oxygen, hydrogen on Cu_2O can be adsorbed on Cu atoms as H with weak bonding.

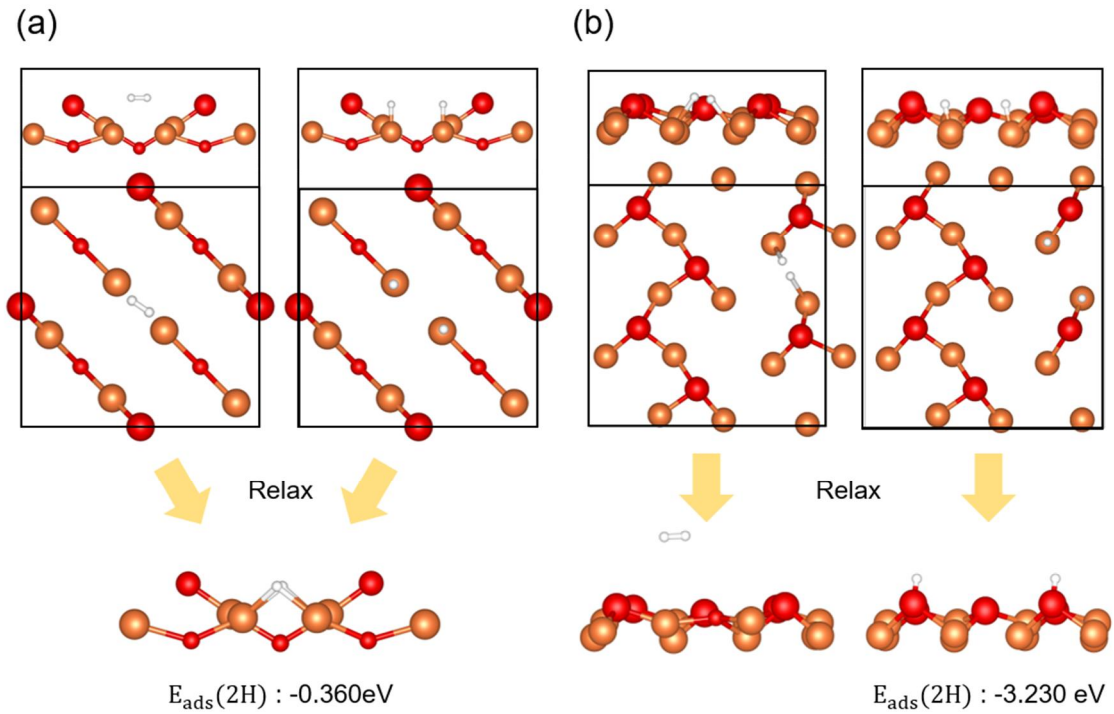

Figure 13. Side (above) and top (below) view of initial configuration of (a) H2 and (b) 2H on CuO. Side view of fully-relaxed final configuration of (c) H2 and (d) 2H on Cu2O. H atoms are strongly trapped on surface oxygen atoms.

To identify the dissociated H can easily migrate on Cu_2O, migration barrier of H is calculated. Because H atoms prefer to bind to active site, one H was placed on active site and the other H was moved to other sites. We considered two type of structures.: One type has a Cu-H-Cu bonds perpendicular to the H bonds at active site (Fig.14a, M structure) and the other type has a Cu-H-Cu bonds parallel to the H bonds at active site, with oxygen underneath the H atom (Fig.14a, I structure). The I structure has a low 2H adsorption energy of -0.413 eV, similar to the energy of the F structure. However, in the case of the M structure, the adsorption energy is -0.875eV, which is about 0.5eV higher than the I and F structures due to hydrogen bond with the surrounding outermost oxygen[36].

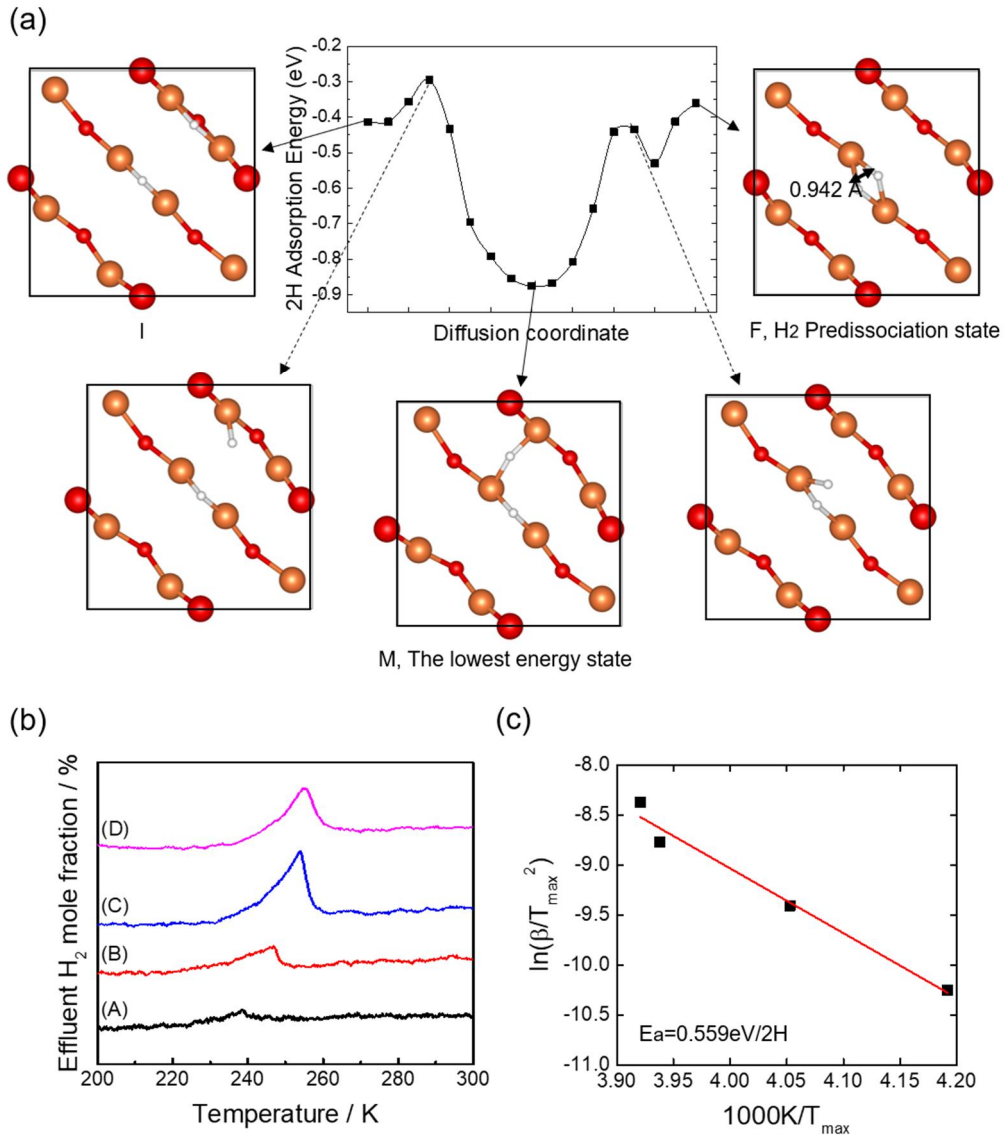

Figure 14. (a) The migration barrier of H atom on Cu2O(100) and structures along the diffusion pathway. (b) H2 TPD spectra using the heating rates of (A) 2K/min, (B) 5K/min, (C) 10K/min and (D) 15K/min. (c) $\mathbf{ln(\Phi/T_{max}^2)}$ versus $\mathbf{1/T_{max}}$ plot from H2 TPD spectra . The slope value is -6.48225.

Since the 2H adsorption energy of the M is lower than that of others, calculated migration barriers of H from M to I and M to F structures are 0.515eV and 0.581eV (Fig.14a) The barrier is low enough for the migration of H atoms under our experimental condition, so on Cu2O(100), hydrogen can be supplied to surface furfural for hydrogen reaction.

The temperature-programmed desorption of hydrogen (H2 TPD) was used to experimentally demonstrate the calculational result on Cu2O. Because H2 TPD trace was observed at around 250K on Cu surface with H2 binding energy of 0.81 eV (ref), H2 TPD experiments were carried out at low temperature(160K~) and were performed with four different heating rates of 2K/min, 5K/min, 10K/min and 15K/min after doping pure H2 on Cu2O with the same doping pressure. Each TPD trace was shown in Figure 2(e). The peak maximum shifts toward slightly higher temperature as the heating rate increases. From the Kissinger equation, a slope of $\ln(\Phi/T_{max}^2)$ versus $1/T_{max}$ plot means an activation energy of H2 divided by the gas constant R[37]. Therefore, the experimental activation energy of H2 on Cu2O was determined to be 0.559 eV from the linear plot of the H2 TPD experiments (Figure 2(f)). The activation energy of TPD is the energy of the rate determining step (RDS) during hydrogen desorption and it is the same with either the adsorption energy of H2 in I structure or the migration barrier of H. Thus, it is expected that the RDS step is hydrogen migration in good agreement with our calculated H migration barrier. Therefore, the TPD result can demonstrate the calculational result that hydrogen can move on the Cu2O surface via Cu atoms, unlike on CuO.

As a result, on CuO(100), it is difficult to supply hydrogen to FAL because the strong binding to the oxygen hinders the transfer of H atoms to FAL. On the contrary, on $Cu_2O(100)$, The adsorbed H atoms cannot be only dissociated but also migrate easily between the Cu because hydrogen can be adsorbed preferentially to the surface Cu atoms rather than O atoms that capture hydrogens. The difference in the behavior of hydrogen contributes to a higher reaction rate in FAL hydrogenation on $Cu_2O(100)$ than on CuO(100). DFT calculation results clearly demonstrate that $Cu_2O(100)$ is a key active species promoting the high activity of FAL hydrogenation due to the selective adsorption and migration behavior of hydrogen as well as high adsorption energy of FAL.

5. Sulfur doped Silicon Anode with fast charging rate

Silicon is one of promising lithium-ion battery because of its much high capacity of 4200mAh/g and abundancy. However, it has some problems of a large volume expansion during lithiation and a low charging rate due to the low ionic and electronic transport. In our experiments, a sulfur doped silicon anode with a hollow shape exhibited very fast Li diffusion and stabilization during Li charging[38]. In particular, the Li diffusion coefficient during lithiation in the first cycle was increased

around several thousand times (Fig.15). Since the diffusion barrier of lithium ion is 0.5eV in Si bulk, there should be a pathway with Li diffusion barrier of almost 0eV. Thus, it was expected that there would be some empty spaces in the S doped Si structure. Considering a variety of sulfur ring structures with various angles and existence of poly-sulfide in the experiment (Fig.15e), I introduced a S doped Si structure in which the empty space is supported by chain-like sulfur.

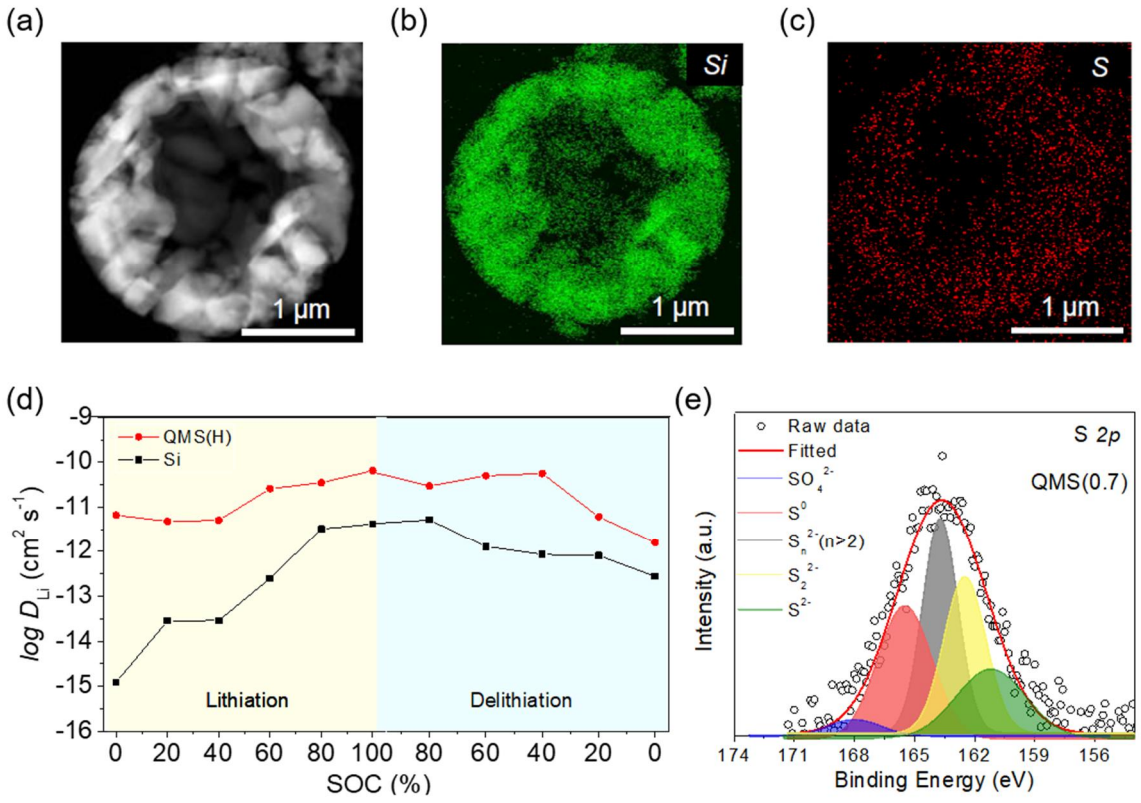

Figure 15. (a) Scanning transmission electron microscopy (STEM) image. Corresponding energy-dispersive X-ray spectroscopy (EDS) maps for (b) Si and (c) sulfur. (d) Calculated diffusion coefficient (D_{Li}) after CV measurement that corresponds to the state after 50 cycles. (e) X-ray Photoelectron spectroscopy results of S 2*p* core-level spectra of QMS.

5.1 Calculational Methods

Ab-initio calculations were performed using the Vienna ab-initio simulation package (VASP) code[21] in the framework of the spin-polarized density functional theory with the projector augmented wave (PAW) method[22]. The exchange-correlation was considered using the generalized gradient approximation of Perdew, Burke, and Ernzerhof (PBE)[23]. The cut-off energy for the plane wave basis set was 350eV. A k-point mesh in the Monkhorst-Pack scheme[24] was set to $1 \times 1 \times 2$ and $2 \times 2 \times 2$

for S doped Si (S_1Si_{255} and S_1Si_{63}, respectively) and $1 \times 1 \times 1$ for the channel structure. The ionic positions of all atoms were fully-relaxed until a force convergence of 0.01 eV $Å^{-1}$ was reached. The pressure applied to the channel depending on the different slab spacing was calculated to be set to allow only ion relaxation without volume change.

Density functional molecular dynamics (DFTMD) simulation was conducted on a canonical ensemble to generate amorphous Si for the interface structure with lithium sulfide particles. The k-point set was set to only the gamma points for $2 \times 2 \times 2$ supercell of Si and the time step was set to 0.5 fs. The temperature was chosen as 1800 K, and the DFTMD simulations were performed for 2.5 ps. To determine the kinetic behaviors of Li-ion in the channel and the interface, we used the climbing image nudged elastic band (cNEB) method[29] to calculate the diffusion barriers of Li-ion on expected diffusion pathways.

5.2 Results and Discussion

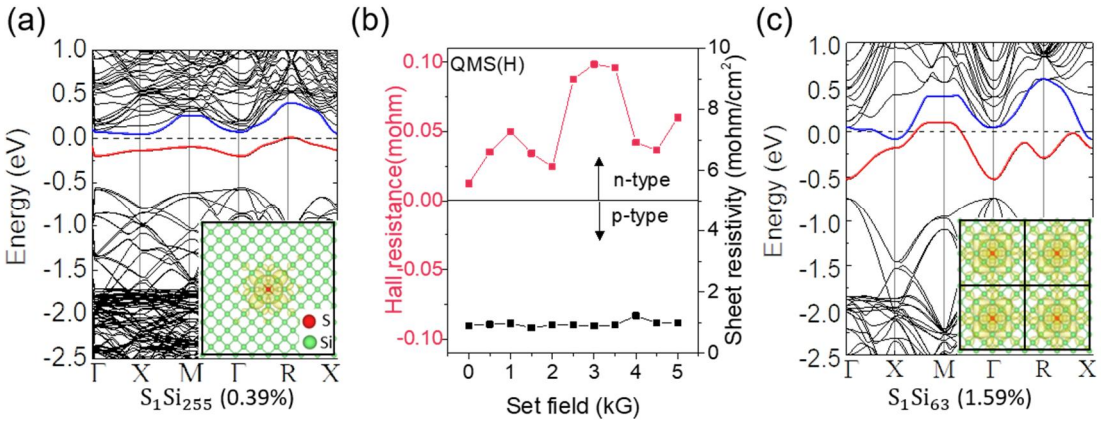

Figure 16. Band structure of S doped Si with different substitution doping concentrations of (a) 0.39%, S_1Si_{255}, and (b) 1.59%, S_1Si_{63}. The charge density distribution at these impurity levels (in the insets) is shown in red and blue lines to intuitively illustrate the contribution of Si to the metallic properties. The isosurface of the density is 0.0005 $\mathbf{e}/Å^3$. (b) Hall effect measurement results of S doped Si.

Sulfur doping on the Si structure produces two electrons than do not participate in the bond because sulfur can form only two bonds, unlike Si, which forms four bonds. Thus, the remaining two electrons create two impurity states below the conduction band minimum (CBM), labeled red and blue lines, and occupy mostly one of the two states. At the low doping concentrations of sulfur (0.39%), the states are far enough apart not to interact with each other and form localized bands. The flat bands just touch the fermi level. (Fig.16c) In case of the high doping concentrations of sulfur (1.59%), a distance

between the impurity states becomes closer and overlap each other. This percolation makes the band dispersion of the states large, and then they are surely across the fermi level and form metallic bands. Thus, S doped Si structure may begin to become metallic from the sulfur doping concentration of about 0.39% and have stronger metallic properties as the dispersion of states is increased by increasing the concentration.

Charge density analysis demonstrates the changes in the metallic properties of Si with different sulfur concentrations at the impurity levels. As shown in insets of Figure 16a and b, the impurity states are constituted by Si states rather than S states as described above. The fact that the impurity levels lies below the CBM indicates S doping has n-type doping character. At low doping concentrations of S (0.39%), only the Si atoms surrounding the S atom contribute to the formation of the localized impurity levels. At the high doping concentrations of S, overlap between localized impurity levels makes the large band dispersion and delocalized state as shown in Figure 16c. This metallic properties by sulfur doping is in good agreement with Thus, the extra electrons can move throughout the Si crystal due to its metallicity, and then the electric conductivity can be improved by improving the mobility of the electrons.

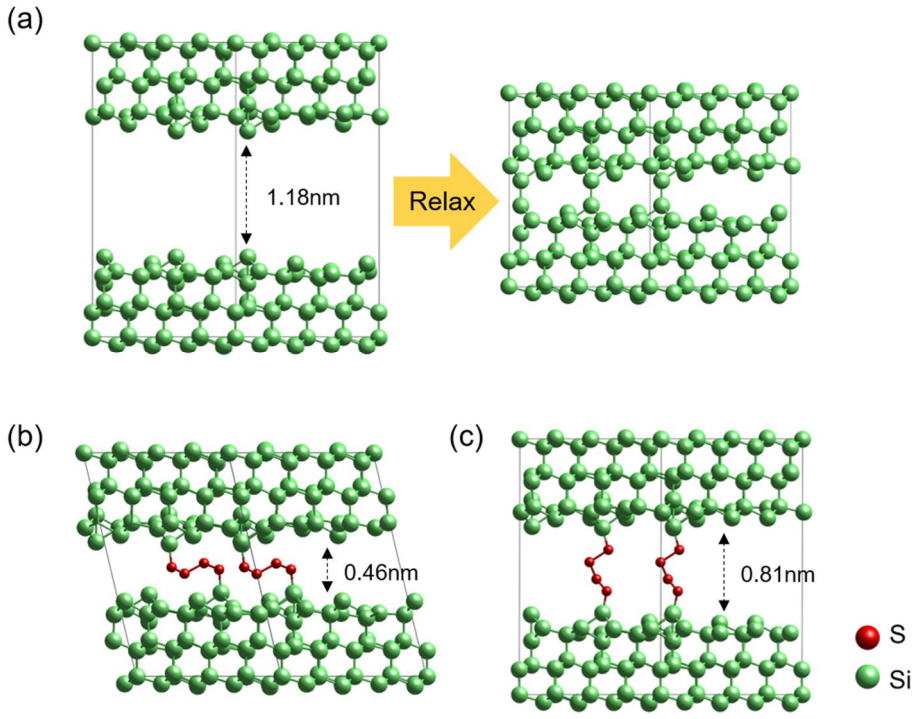

Figure 17. (a) Initial channel structure with slab spacing of 1.18 nm (left) and its fully-relaxed channel structure without sulfur chains (right), (b) Fully-relaxed structure with the slab spacing of 0.46 nm from initial spacing range of 0.51 to 0.70 nm with sulfur chains. (c) Fully-relaxed structure with the slab spacing of 0.81 nm from initial spacing range of 0.80 to 0.99 nm.

The difference in conductivity from the change of mobility and metallic properties according to the S doping concentration is consistent with the experimental data. (Fig.16b) The doping concentration of 0.7% sulfur used in our experiments was high enough to make S doped Si quasi-metallic. Therefore, based on our calculation results, we believe that the sulfur doping leads to the metallic properties with n-doping character and the improvement of conductivity of QMS.

The chain-like sulfur can sustain the spacing between Si surfaces with the intact chain shape. Using the adatoms from the most stable Si(111) reconstruction structure, DFT calculations were performed on Si (111) structures in which the sulfur chain connects the adatoms of each surface. In the absence of the sulfur fusion, channel with 1 nm of slab spacing cannot be maintained because Si atoms having dangling bonds on both Si surface have a strong attraction and restore its bulk structure. (Fig.17a). However, the chain-like sulfurs are able to bear the Si planes facing each other and sustain interplanar spacings with initial spacing range from 0.51nm to 0.99nm. The sulfur chain can be maintained in various spacing range with a high flexibility and is robust enough to hold up the structure at pressure as high as 14 kbar (Fig. 17b,c, Fig.18a). Li diffusion through the channel has a very low barrier of 0.11eV (Fig.18b) and can account for the high Li diffusion coefficient observed in the experiment.

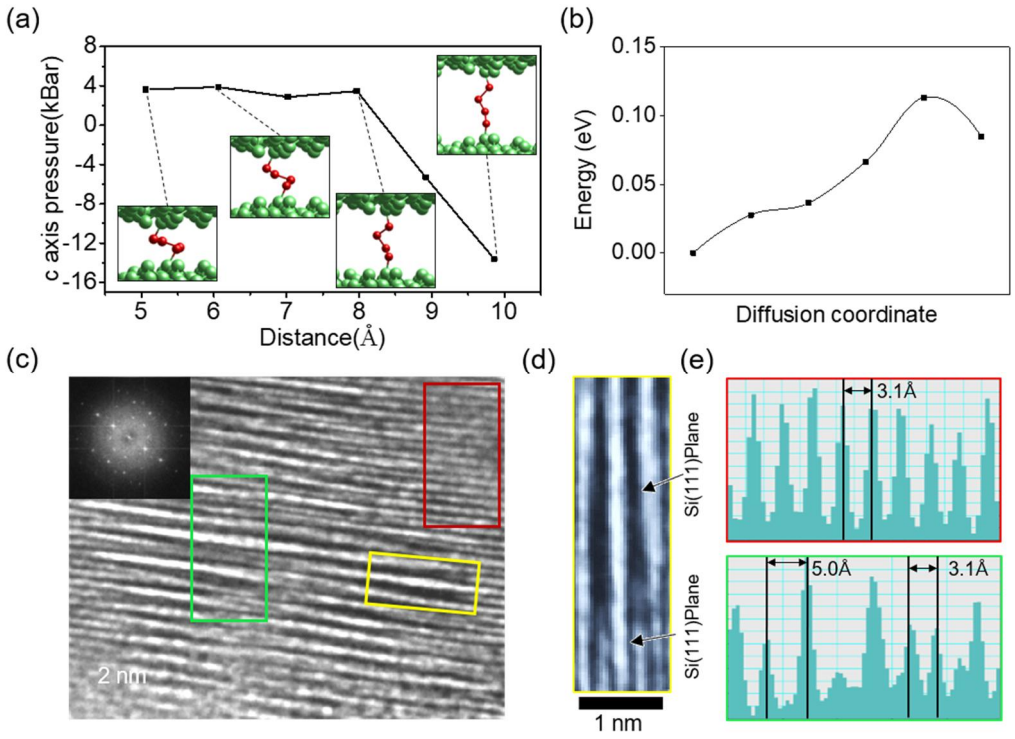

Figure 18. (a) Sulfur chain structure under applied pressure depending on different channel sizes, as calculated by DFT. (b) Diffusion barrier of Li ion through the channel center. (c) HR-TEM image of the hollow S doped Si (inset: corresponding fast fourier transform image). (d) Enlarged TEM image showing column formation between characteristic Si (111) planes. (e) Intensity profiles of selected areas in (c).

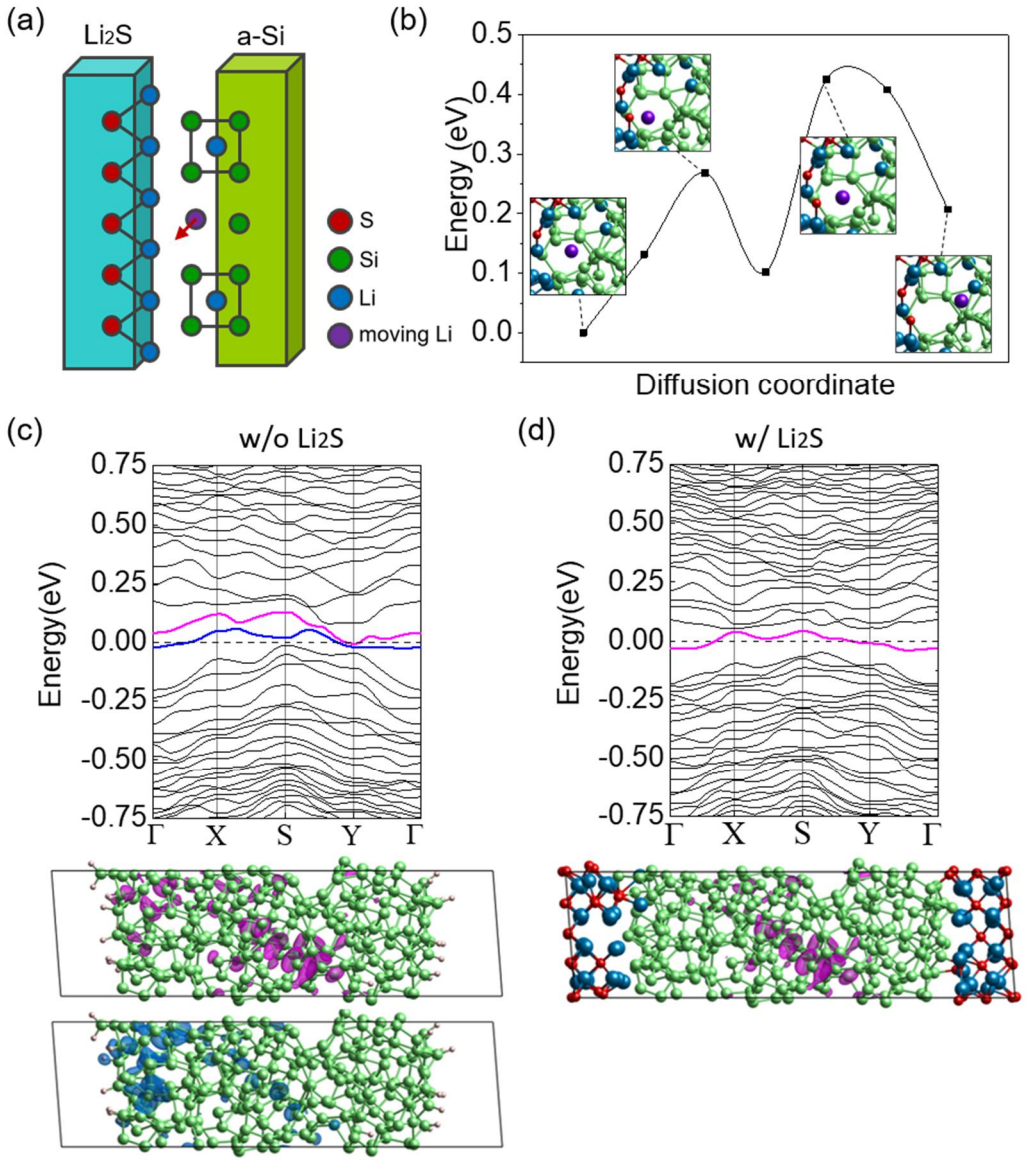

Figure 19. (a) Schematic illustration of Li diffusion path at an interface between lithium sulfide (**Li_2S**) and amorphous Si (a-Si). (b) Diffusion energy barrier for Li-ion via the interface path. (c) Band structure of the interface structure of H-passivated amorphous Si without **Li_2S** (Fermi level (E_f) set to zero) and charge density plot at CBM state (red line). White atoms on the silicon surface are hydrogen atoms. (d) Band structure of the interface structure of a-Si with **Li_2S** and charge density plot at the state across the E_f(red line). Isosurface of the density is 0.0007 $\mathbf{e}/\text{Å}^3$.

The channel structure in the hollow Si is identified by high-resolution transmission electron microscopy (HR-TEM). The fully-relaxed structures in Figure 17b and c show that the channel structures with four sulfur atoms are most stable with the slab spacings of 0.46nm and 0.81nm. HR-TEM image and its intensity profiles are in good agreement with our calculations; spacings from the

sulfur chains are parallel to (111) planes in the S doped Si and distribute mostly in 0.50–0.72 nm compared to 0.31 nm of lattice constant for Si (111) planes (Fig.18c,d,e). Therefore, we can suggest that sulfur doping contributes to a formation of empty channel space during clustering Si fragment and the channel supported by sulfur makes Li diffusion thousands of times faster than that in undoped Si.After the first cycle, it is expected that lithium sulfide like structures maintain the improved Li diffusivity. During the first cycle, the sulfur chain is collapsed due to formation of Li-Si bonds and Li_2S-like structure is formed. The crystalline Si also becomes amorphous. At interface between Li_2S and amorphous Si, Li_2S tends to be close to the amorphous Si, but is not flexible enough to fill in a vacant space of the Si surface as shown in Figure 19a. Thus, I considered the space as a Li diffusion pathway after the sulfur chain collapsed. The Li diffusion through the expected pathway has a lower barrier of 0.32 eV than that in crystalline Si, in good agreement with the experimental result (Fig.19b).

The lithium sulfide like structure also contributes metallicity of the amorphous Si. In the absence of Li_2S, the amorphous Si has a state just above the fermi level and charge density profile clearly shows that internal Si contributes to the state (Fig.19c, red line). In interface between amorphous Si and Li_2S, the state of internal amorphous Si is occupied by an electron provide by Li_2S. Because the state occupied by the charge transfer overlaps with the fermi level, the S doped Si can have the metallic property (Fig.19d, red line). The charge density plots demonstrate that the CBM state of the amorphous Si and the metallic state of the interface originates from the same internal Si. The other metallic band can be explained with metallic surface states of the amorphous silicon due to dangling bonds of surface Si, which has weaker metallic property (Fig.19c, blue line). Therefore, the calculated low Li diffusion barrier and Si metallicity, which are in good agreement with the experimental Li diffusivity, support the prediction about the contribution of lithium sulfide.

6. Conclusion

In this paper, I covered the analysis and results for various nanostructures using DFT. DFT is efficient to analyze for specific properties caused by structural change due to doping or reduction and to determine the actual formation possibilities of structural designs for specific properties. In addition, carrier diffusion or band-gap tuning for photocatalysts and reaction pathway or activation energy analysis for catalysts are also possible. Using these benefits of DFT calculation, I suggest the host Ti doping effect which enables donor-donor co-doping in hematite, Cu2O catalyst for hydrogenation reaction and sulfur chain structure that makes the specific pathway for Li diffusion in crystalline silicon.

REFERENCES

1. Kennedy, J. H., Photooxidation of Water at α-Fe_2O_3 Electrodes. *Journal of The Electrochemical Society* **1978,** *125* (5).
2. Marusak, L. A.; Messier, R.; White, W. B., Optical absorption spectrum of hematite, αFe2O3 near IR to UV. *Journal of Physics and Chemistry of Solids* **1980,** *41* (9), 981-984.
3. Brillet, J.; Yum, J.-H.; Cornuz, M.; Hisatomi, T.; Solarska, R.; Augustynski, J.; Graetzel, M.; Sivula, K., Highly efficient water splitting by a dual-absorber tandem cell. *Nature Photonics* **2012,** *6*, 824.
4. Murphy, A. B.; Barnes, P. R. F.; Randeniya, L. K.; Plumb, I. C.; Grey, I. E.; Horne, M. D.; Glasscock, J. A., Efficiency of solar water splitting using semiconductor electrodes. *International Journal of Hydrogen Energy* **2006,** *31* (14), 1999-2017.
5. Sivula, K.; Le Formal, F.; Grätzel, M., Solar Water Splitting: Progress Using Hematite (α-Fe2O3) Photoelectrodes. *ChemSusChem* **2011,** *4* (4), 432-449.
6. Dare-Edwards, M. P.; Goodenough, J. B.; Hamnett, A.; Trevellick, P. R., Electrochemistry and photoelectrochemistry of iron(Ⅲ) oxide. *Journal of the Chemical Society, Faraday Transactions 1: Physical Chemistry in Condensed Phases* **1983,** *79* (9), 2027-2041.
7. Morin, F. J., Electrical Properties of αFe_2O_3 and αFe_2O_3 Containing Titanium. *Physical Review* **1951,** *83* (5), 1005-1010.
8. Bosman, A. J.; van Daal, H. J., Small-polaron versus band conduction in some transition-metal oxides. *Advances in Physics* **1970,** *19* (77), 1-117.
9. Iordanova, N.; Dupuis, M.; Rosso, K. M., Charge transport in metal oxides: A theoretical study of hematite α-Fe2O3. *The Journal of Chemical Physics* **2005,** *122* (14), 144305.
10. Glasscock, J. A.; Barnes, P. R. F.; Plumb, I. C.; Savvides, N., Enhancement of Photoelectrochemical Hydrogen Production from Hematite Thin Films by the Introduction of Ti and Si. *The Journal of Physical Chemistry C* **2007,** *111* (44), 16477-16488.
11. Chatman, S.; Pearce, C. I.; Rosso, K. M., Charge Transport at Ti-Doped Hematite (001)/Aqueous Interfaces. *Chemistry of Materials* **2015,** *27* (5), 1665-1673.
12. Zhou, Z.; Huo, P.; Guo, L.; Prezhdo, O. V., Understanding Hematite Doping with Group IV Elements: A DFT+U Study. *The Journal of Physical Chemistry C* **2015,** *119* (47), 26303-26310.
13. Smart, T. J.; Ping, Y., Effect of defects on the small polaron formation and transport properties of hematite from first-principles calculations. *Journal of Physics: Condensed Matter* **2017,** *29* (39), 394006.
14. Korotkov, R. Y.; Gregie, J. M.; Wessels, B. W., Codoping of wide gap epitaxial Ⅲ-Nitride semiconductors. *Opto-electronics Review* **2002,** *10* (4), 243-249.
15. Kröger, F. A.; Vink, H. J., Relations between the concentrations of imperfections in solids. *Journal of Physics and Chemistry of Solids* **1958,** *5* (3), 208-223.
16. Janotti, A.; Wei, S.-H.; Zhang, S. B., Donor–donor binding in semiconductors: Engineering

shallow donor levels for ZnTe. *Applied Physics Letters* **2003,** *83* (17), 3522-3524.

17. Wang, L.; Maxisch, T.; Ceder, G., Oxidation energies of transition metal oxides within the GGA+U framework. *Physical Review B* **2006,** *73* (19), 195107.

18. Lee, J.; Han, S., Thermodynamics of native point defects in α-Fe2O3: an ab initio study. *Physical Chemistry Chemical Physics* **2013,** *15* (43), 18906-18914.

19. Reuter, K.; Scheffler, M., Composition and structure of the RuO_2(110) surface in an O_2 and CO environment: Implications for the catalytic formation of CO_2. *Physical Review B* **2003,** *68* (4), 045407.

20. Stull, D. R.; Prophet, H., *JANAF thermochemical tables [electronic resource] / D.R. Stull and H. Prophet, project directors*. U.S. Dept. of Commerce, National Bureau of Standards: Washington, D.C, 1971.

21. Kresse, G.; Furthmüller, J., Efficient iterative schemes for ab initio total-energy calculations using a plane-wave basis set. *Physical Review B* **1996,** *54* (16), 11169-11186.

22. Kresse, G.; Joubert, D., From ultrasoft pseudopotentials to the projector augmented-wave method. *Physical Review B* **1999,** *59* (3), 1758-1775.

23. Perdew, J. P.; Burke, K.; Ernzerhof, M., Generalized Gradient Approximation Made Simple. *Physical Review Letters* **1996,** *77* (18), 3865-3868.

24. Monkhorst, H. J.; Pack, J. D., Special points for Brillouin-zone integrations. *Physical Review B* **1976,** *13* (12), 5188-5192.

25. Morin, F. J., Magnetic Susceptibility of αFe_2O_3 and αFe_2O_3 with Added Titanium. *Physical Review* **1950,** *78* (6), 819-820.

26. Finger, L. W.; Hazen, R. M., Crystal structure and isothermal compression of Fe2O3, Cr2O3, and V2O3 to 50 kbars. *Journal of Applied Physics* **1980,** *51* (10), 5362-5367.

27. Zhang, M.; Luo, W.; Li, Z.; Yu, T.; Zou, Z., Improved photoelectrochemical responses of Si and Ti codoped α-Fe2O3 photoanode films. *Applied Physics Letters* **2010,** *97* (4), 042105.

28. Nolan, M.; Elliott, S. D., The p-type conduction mechanism in Cu2O: a first principles study. *Physical Chemistry Chemical Physics* **2006,** *8* (45), 5350-5358.

29. Henkelman, G.; Uberuaga, B. P.; Jónsson, H., A climbing image nudged elastic band method for finding saddle points and minimum energy paths. *The Journal of Chemical Physics* **2000,** *113* (22), 9901-9904.

30. Maimaiti, Y.; Nolan, M.; Elliott, S. D., Reduction mechanisms of the CuO(111) surface through surface oxygen vacancy formation and hydrogen adsorption. *Physical Chemistry Chemical Physics* **2014,** *16* (7), 3036-3046.

31. Soon, A.; Todorova, M.; Delley, B.; Stampfl, C., Thermodynamic stability and structure of copper oxide surfaces: A first-principles investigation. *Physical Review B* **2007,** *75* (12), 125420.

32. Tasker, P. W., The stability of ionic crystal surfaces. *Journal of Physics C: Solid State Physics* **1979,** *12* (22), 4977-4984.

33. Sitthisa, S.; Pham, T.; Prasomsri, T.; Sooknoi, T.; Mallinson, R. G.; Resasco, D. E.,

Conversion of furfural and 2-methylpentanal on Pd/SiO2 and Pd–Cu/SiO2 catalysts. *Journal of Catalysis* **2011,** *280* (1), 17-27.

34. Sitthisa, S.; Sooknoi, T.; Ma, Y.; Balbuena, P. B.; Resasco, D. E., Kinetics and mechanism of hydrogenation of furfural on Cu/SiO2 catalysts. *Journal of Catalysis* **2011,** *277* (1), 1-13.

35. Sakong, S.; Groß, A., Dissociative adsorption of hydrogen on strained Cu surfaces. *Surface Science* **2003,** *525* (1), 107-118.

36. Rao, L.; Ke, H.; Fu, G.; Xu, X.; Yan, Y., Performance of Several Density Functional Theory Methods on Describing Hydrogen-Bond Interactions. *Journal of Chemical Theory and Computation* **2009,** *5* (1), 86-96.

37. Kissinger, H. E., Reaction Kinetics in Differential Thermal Analysis. *Analytical Chemistry* **1957,** *29* (11), 1702-1706.

38. Ryu, J.; Seo, J. H.; Song, G.; Choi, K.; Hong, D.; Wang, C.; Lee, H.; Lee, J. H.; Park, S., Infinitesimal sulfur fusion yields quasi-metallic bulk silicon for stable and fast energy storage. *Nature Communications* **2019,** *10* (1), 2351.